Spring 2021

A New Method for Estimating the Physical Characteristics of Martian Dust Devils

Shelly Cahoon Mann
Old Dominion University, scaho001@odu.edu

A NEW METHOD FOR ESTIMATING THE PHYSICAL CHARACTERISTICS OF MARTIAN DUST DEVILS

by

Shelly Cahoon Mann
B.S. May 1995, Old Dominion University

A Thesis Submitted to the Faculty of
Old Dominion University in Partial Fulfillment of the
Requirements for the Degree of

MASTER OF SCIENCE

AEROSPACE ENGINEERING

OLD DOMINION UNIVERSITY
May 2021

Approved by:

Robert L. Ash (Director)

Colin P. Britcher (Member)

Shizhi Qian (Member)

ABSTRACT

A NEW METHOD FOR ESTIMATING THE PHYSICAL CHARACTERISTICS OF MARTIAN DUST DEVILS

Shelly Cahoon Mann
Old Dominion University, 2021
Director: Dr. Robert L. Ash

Critical to the future exploration of Mars is having a detailed understanding of the atmospheric environment and its potential dangers. The dust devil is one of these potential dangers. The transport of dust through saltation is believed to be the driving mechanism responsible for Martian weather patterns. The two primary mechanisms for dust transport are dust storms and dust devils. Dust devils on Mars are a frequent occurrence with one in five so called giant dust devils being large enough to leave scars on the surface that are visible from space. Due to the thin atmosphere, winds of 60 mph would feel more like 6 mph terrestrial winds; however, the saltation of dust particles could pose a threat to structures and equipment. Materials for permanent structures and equipment will need to be abrasion resistant, and the possible solenoidal effects of the columnar vortices, such as triboelectric charging and induced magnetic fields, will need to be well understood. Thus, it would be useful to have a method of quantifying the physical properties of Martian dust devils.

This work has endeavored to provide such a method by employing an improved Rankine vortex model developed by Ash, Zardadkhan, and Zuckerwar (2011, 2013) which agreed well with terrestrial field measurements. Atmospheric differences between Earth and Mars are profound and limited or incomplete in situ data for Martian dust devil events presented a challenge when applying the Ash-Zardadkhan-Zuckerwar method; however, through an inclusive representation of the atmosphere, its thermodynamic properties, and proven scientific inferences of other necessary atmospheric properties, this work has developed a useful tool to aid in the safe advancement of large-scale planetary exploration.

This work is dedicated to my family:
for their understanding and encouragement.

ACKNOWLEDGMENTS

I would like to express my enormous appreciation and gratitude to my advisor, Dr. Robert L. Ash, whose guidance, encouragement, and patience has made this work possible. He is a true mentor and educator, and it has been a privilege to learn from him these last few years. I would also like to acknowledge Dr. William Moore and Dr. Nicholas Heavens, both of Hampton University, for lending their expertise on more than one occasion and pointing me in the right direction. My special thanks go to Dr. Colin Britcher and Dr. Shizhi Qian for their guidance and support, and for their service on my thesis committee. Finally, to my fellow graduate students in the Aerospace Engineering program, thank you; the camaraderie and support has been an invaluable part of this journey.

NOMENCLATURE

a_{vib}	vibrational absorption coefficient
C_n	Sutherlands constant for a gas component
c	speed of sound
$c_p{}^0$	unfrozen specific heat constant pressure
$c_v{}^0$	unfrozen specific heat constant volume
$c_p{}^\infty$	frozen specific heat constant pressure
$c_v{}^\infty$	frozen specific heat constant volume
c_{vib}	vibrational contribution to specific heat
C/L	center line
f_c	collision frequency
f_r	relaxation frequency
g	gravitational constant
h_{max}	stagnation plane height
k	forward reaction rate
k_b	reverse reaction rate
L_s	sun aerocentric longitude
$Matm$	Mars atmosphere
m_{gas}	mass of a gas component
M_{gas}	molar mass of a gas component
n_{gas}	number of moles of a gas component
N_{vib}	number of vibrational degrees of freedom
P	pressure
P_r	atmospheric reference pressure
P_{sat}	saturated vapor pressure
p_{ice}	saturated vapor pressure of ice

p_{liq}	saturated vapor pressure of liquid water
p_{vap}	vapor pressure
q	specific humidity (humidity ratio)
q_{sat}	saturation specific humidity (saturation humidity ratio)
r	radius
r_{core}	radius of the dust devil core
R_Γ	circulation-based Reynolds number
R_u	universal gas constant
R_{spec}	gas specific gas constant
RH	relative humidity
S	relaxation strength
Sol	n^{th} day of a mission
T_t	triple point temperature of H_2O
T	temperature
$\boldsymbol{v}$	velocity vector
VMR	volume mixing ratio
V_θ	azimuthal or swirl velocity
w_{gas}	molar mass fraction of a gas component
X_i	mole fraction of a gas compoent
x_h	mole fraction of water vapor
z	condensation height of an atmospheric column
α	dry adiabatic lapse rate
η_p	pressure relaxation coefficient
η_v	volume viscosity coefficient
∞	far-field, ambient, or local condition
γ	specific heat ratio
Γ_0	maximum circulation of the dust devil

μ	dynamic viscosity
ν	kinematic viscosity
ν_{turb}	turbulent viscosity
ω	angular rotation rate
Ω	potential energy
ρ	density
σ	shear stress
τ_{PS}	constant pressure isentropic relaxation time
τ_{VS}	constant volume isentropic relaxation time
τ_{VT}	constant volume and temperature relaxation time
θ_j	vibrational relaxation temperature
ω	angular rotation rate

TABLE OF CONTENTS

Page

Page

LIST OF TABLES

LIST OF FIGURES

CHAPTER 1

INTRODUCTION

One of the main challenges to fully understanding the impact that dust devils will have on the future of Mars exploration is accurate data. To develop structural design standards and systems requirements, reliable transient aerodynamic load data are needed. Starting with the Viking Landers in 1976, we have been able to collect evidence of dust devil activity, through both direct and indirect observation (Thomas and Gierasch, 1985). Indirectly, the presence of dust devils can be inferred on the surface by the detection of pressure drop events that last at least 10 seconds or more in conjunction with a change in wind direction. Viking 1 and 2 and Mars Pathfinder landers (MPF) recorded 145 dust devil events using this indirect observation method, and many more have been imaged from orbiters providing valuable information on scale and frequency (Balme and Greeley, 2006). The Phoenix Mars Lander (PML) identified 502 convective vortices, indirectly, during its 151-sol mission (Ellehoj et al., 2010). A great deal has been learned about the scale, seasonal variations, diurnal activity, and geographic distribution of Martian dust devils (Balme and Greeley, 2006). However, it is not possible presently to reliably estimate the strength and potential threats using mathematical models and observation. Improved methods employing existing data to better understand the behavior and associated engineering considerations from dust devils and large-scale dust storms are needed.

Like all cyclonic flows, dust devils have well-defined Rankine-vortex-like tangential velocity distributions (Sinclair, 1973). Unlike waterspouts, tornadoes, and hurricanes, terrestrial and Martian dust devils result primarily from thermally induced buoyant phenomena. Terrestrial dust devils are commonly observed in hot dry climates but rarely occur at scales large enough to threaten structures. On Mars, however, as evidenced by dust devil tracks visible from space, these events can be at least an order of magnitude larger in scale and with daily average occurrence levels as high as 1 event per square kilometer per sol (Jackson, 2018). The geospatial ability to estimate probability of occurrence and likely strength is critical to understanding the threat to landers, solar arrays, and larger surface structures. Sinclair (1973), through his measurements and observations of three dust devils in the desert near Tucson Arizona in 1962, found that the primary axial structure of dust devils could be approximated employing the two-

zone Rankine vortex model—a rigidly rotating inner core surrounded by an irrotational, potential vortex annular shell.

Rankine's 1858 theoretical vortex model was a result of his efforts to describe the velocity profile of observed vortical flows exhibiting the behavior of a potential flow while avoiding the problem of infinite velocity at the centerline. There is no physical basis for this one-dimensional Rankine vortex flow field model, and despite this, it approximates the tangential or swirl velocity profiles in tornadoes and dust devils (S. Gillmeier et al., 2018; Sinclair, 1973). Since the early 1900s, many have sought to achieve a physical process or mechanism model describing the evolution of this complex flow field through exact solutions to the Navier-Stokes equations. The results of these efforts produced the Lamb-Oseen vortex (Lamb, 1932), Görtler vortex (Görtler, 1954), Sullivan Vortex (Sullivan, 1959), Burgers-Rott vortex (Burgers, 1948; Rott, 1958), and the even more recent Baker vortex (Baker and Sterling, 2017). While all were important developments, each model had limitations and situational applicability. Currently, the Rankine, Sullivan, and Burgers-Rott models are the most widely employed approximations for large-scale vortices like tornadoes and hurricanes. The Sullivan, Burgers-Rott, and more recent Baker models attempted to include the radial and axial-velocity components and were successful to a degree over differing but limited flow field height ranges (S. Gillmeier et al., 2018). Based on this and Sinclair's experimental dust devil observations, a Rankine model is a useful starting point.

While the Rankine vortex velocity profile is continuous, the interface between the inner and outer flow regions creates a shearing discontinuity that requires an instantaneous transition to an inviscid flow. Since viscosity does not vanish in real fluids, accounting for how the flow could transition or "jump" from a rigidly rotating fluid column to a potential vortex in the Rankine model has remained the underlying challenge. Ash, Zardadkhan, and Zuckerwar (2011) identified a non-equilibrium pressure mechanism for balancing the centrifugal and shear stress forces, resulting in a Rankine vortex analog. Table 1 below shows a simple comparison between the Rankine vortex model and the Ash-Zardadkhan-Zuckerwar model (abbreviated as AZZ). Note that the AZZ model predicts a smooth velocity profile and a pressure coefficient that is twice the magnitude of the Rankine Vortex. The prediction of a larger pressure deficit correlates directly to an increased intensity, or strength of a vortex. Another key difference between the two models is the assumption by Rankine of constant angular velocity in the inner core; the Ash,

Zardadkhan, and Zuckerwar (2011) study showed that the inner core angular velocity was not a constant.

Vortex Model	**Azimuthal Velocity**[1]	**Pressure Distribution**	**Pressure Coefficient**[2]
Rankine	$V_\theta(r) = \frac{V_{\theta,max}}{\mathrm{r}_{core}}\mathrm{r} \quad \rightarrow \mathrm{r} \le \mathrm{r}_{core}$ $V_\theta(r) = \frac{V_{\theta,max}\,\mathrm{r}_{core}}{r} \quad \rightarrow \mathrm{r} > \mathrm{r}_{core}$	$P_\infty - P = \rho {V_{\theta,max}}^2$	$C_P = -2$
AZZ	$V_\theta(r) = 2V_{\theta,max}\frac{(r/\mathrm{r}_{core})}{(r/\mathrm{r}_{core})^2 + 1}$	$P_\infty - P = 2\rho {V_{\theta,max}}^2$	$C_P = -4$

Table 1: Vortex model comparison; Rankine and AZZ

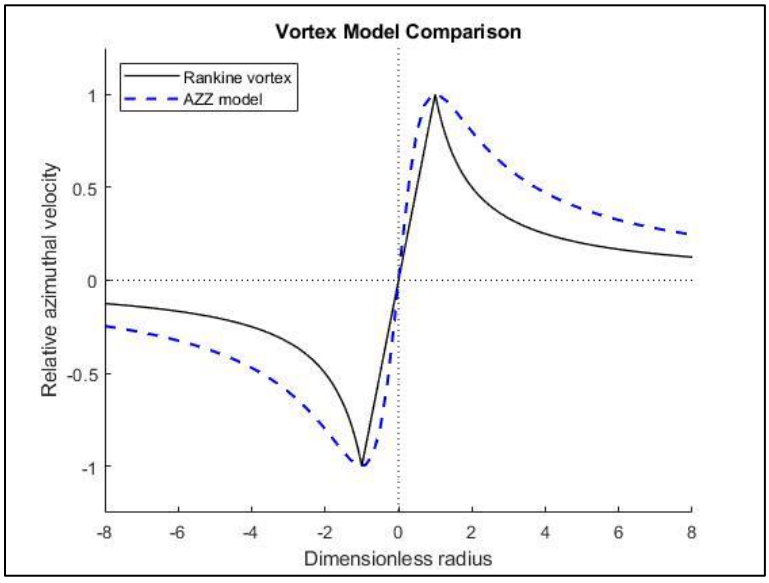

Figure 1: A comparison of velocity profiles; Rankine Vortex and AZZ model.

[1] $V_{\theta,max}$ is the maximum swirl, or tangential velocity at the edge of the inner core; r_{core} is the radius of the inner core.

[2] The Pressure coefficient is defined as $C_P = \frac{P - P_\infty}{\frac{1}{2}\rho_\infty V_{\theta,max}}$.

The model developed by Ash, Zardadkhan, and Zuckerwar offers an improvement over the Rankine vortex model. It also has the benefit of describing this flow as a real physical process by showing that non-equilibrium pressure forces provide the mechanism for maintaining the vortex structure. Furthermore, as will be discussed in the coming chapter, their model successfully identified a structural stagnation plane, allowing for the prediction of an estimated maximum height for ground-coupled vortical flows, such as dust devils.

1.1 A Non-equilibrium Approach

Zuckerwar, and Ash (2006, 2009) utilized Hamilton's Principle of Least Action to introduce molecular non-equilibrium processes in the Navier-Stokes equation. This model accounts for non-equilibrium pressure forces on otherwise incompressible flow utilizing classical spectral acoustic absorption data to define and characterize numerically temperature and moisture-dependent, pressure relaxation behavior in air. Extending the earlier work, Ash, Zardadkhan, and Zuckerwar (2011), incorporated non-equilibrium pressure to model the structure of an axial vortex and subsequently, Ash and Zardadkhan (2013) further extended the approach to large-scale, ground-coupled, rotating fluid columns. Those theoretical estimates agreed with terrestrial field measurements (Sinclair, 1973), validating their model. The resulting velocity profile was Rankine-like but with a key difference: the predicted maximum pressure deficit being twice the magnitude predicted by the Rankine model. Additionally, their exact solutions led to relations for estimating key physical circulation-based parameters such as maximum swirl velocity and maximum vortex column height. This work will show how incorporation of non-equilibrium pressure forces in the solution of the Navier-Stokes equations can be applied to dust devils on Mars. Incorporation of the atmospheric state and its associated thermodynamic properties, along with plausible scientific estimates when required, have enabled an assessment of this approach. In essence, a useful approach needed to safely advance planetary exploration has been developed herein.

1.2 The Non-equilibrium Dust Devil Model

Zuckerwar and Ash (2006) developed an analytical formulation to describe the volume viscosity in fluids by applying Hamilton's Principal of Least Action incorporating non-

equilibrium molecular states. Their variational approach produced the following modified Navier-Stokes equation, where $\rho, \boldsymbol{v}$, Ω, μ, and P are respectively, density, velocity, potential energy, dynamic viscosity, and pressure:

$$\rho \frac{D\boldsymbol{v}}{Dt} = -\nabla\left(1 - \eta_p \frac{D}{Dt}\right) P - \rho\nabla\Omega + \nabla\left[\left(\eta_v - \frac{2}{3}\mu\right)\nabla \cdot \boldsymbol{v}\right] + \nabla \times (\mu\nabla \times \boldsymbol{v}) + 2[\nabla \cdot (\mu\nabla)]\boldsymbol{v}. \quad (1.1)$$

Here, the traditional volume viscosity term, η_v, is proportional to the dilatation rate, and the pressure relaxation term, scaled using pressure relaxation coefficient, η_p, produced a proportional relation based on the gradient of the material rate of change of pressure. Subsequently, by allowing for acoustic radiation, Ash, Zardadkhan and Zuckerwar (2011) successfully incorporated the non-equilibrium pressure gradient forces in an exact viscous model for a steady-state axial vortex with specified circulation. After incorporating non-equilibrium pressure forces, the velocity and pressure distributions for these incompressible axial vortices could be written:

$$v_\theta(r) = 2v_{\theta,max} \frac{\frac{r}{r_{core}}}{\left(\frac{r}{r_{core}}\right)^2 + 1} \quad (1.2)$$

and

$$P(r) = P_\infty - 4\rho \frac{\nu}{\eta_p} \frac{1}{\left(\frac{r}{r_{core}}\right)^2 + 1} \quad (1.3)$$

where,

$$v_{\theta,max} = \frac{\Gamma_o}{4\pi r_{core}} = \sqrt{2\frac{\nu}{\eta_p}}, \quad (1.4)$$

and

$$r_{core} = \frac{R_\Gamma}{2}\sqrt{\frac{\nu\eta_p}{2}}. \quad (1.5)$$

The maximum pressure deficit was:

$$|\Delta P_{max}| = 4\rho\frac{\nu}{\eta_p}, \tag{1.6}$$

with circulation-based Reynolds number

$$R_\Gamma = \frac{\Gamma_o}{2\pi\nu}. \tag{1.7}$$

The maximum height of the dust devil column was approximately

$$h_{max} = \frac{1.394}{\eta_p\omega}\sqrt{\frac{\nu}{\omega}}, \tag{1.8}$$

where the angular rotation rate on the axis is

$$\omega = \frac{2v_{\theta,max}}{r_{core}}. \tag{1.9}$$

Virtually all columnar vortices occurring in nature are turbulent. Consequently, turbulence must be considered. On the basis of the severity of the radial strain rates imposed near the "Rankine vortex core zone," Ash has argued that turbulent vortices create anisotropic turbulent Reynolds stresses that can be approximated utilizing a simple eddy viscosity based anisotropic turbulence model (Ash, Zardadkhan, 2021). The earlier axial vortex study by Ash, Zardadkhan, and Zuckerwar (2011) found that accounting for turbulence using a turbulent eddy viscosity, ν_{turb} , produced results in good agreement with measured data, justifying the replacement of kinematic viscosity, ν , with ν_{turb} in the relations (1.3)-(1.8). The turbulent eddy viscosity is the eddy viscosity plus the kinematic viscosity. Successful application of the non-equilibrium model to Martian dust devils should produce a similarly realistic ratio of ν_{turb}/ν .

After examining the Martian environment to obtain the necessary thermophysical characteristics, four documented dust devil encounters observed by the Mars Phoenix Lander, with accompanying pressure and temperature data (M.D. Ellehoj, et al., 2010), have been employed to demonstrate the utility of this model in estimating Mars dust devil intensity and

pertinent physical characteristics. The observation day (Sol), time of year (areocentric longitude, Ls), observed minimum pressure ($\Delta P_{C/L}$) and associated ambient temperature and pressure for those encounters are summarized in Table 2. Provided realistic ratios are achieved; this method can be a useful tool to analyze dust devil events measured by past, present, and future surface, or rover mounted instruments, as well as those captured remotely in images from orbit.

Sol (mission)	**L_s** areocentric longitude	**$\Delta P_{C/L}$** Pa	**T_∞** K	**P_∞** Pa
90	118	2.58	240	765.4
95	120	3.56	240	752.5
118	131	2.37	228	739.5
136	140	2.51	227	727

Table 2. Observed dust devils at Phoenix Mars landing site.

CHAPTER 2

THE MARTIAN ATMOSPHERIC ENVIRONMENT

Terrestrial and Martian dust devils occur in vastly different environments based on atmospheric composition, surface gravity and associated ambient conditions. Those conditions must certainly result in major differences in nonequilibrium core behavior based on η_p. Terrestrial atmospheric and associated thermophysical properties have been measured extensively, along with the underlying relative humidity-based acoustic transmission data, enabling estimation of the pressure relaxation coefficient, η_p, with a high degree of confidence. Phoenix Mars Lander (PML) instruments included a Thermal and Electrical Conductivity Probe, incorporating a Relative Humidity sensor (TECP RH) that was operational throughout the Phoenix mission (Fischer, et al, 2019); however, it did not transmit measurements continuously due to its location on the lander and to competing data throughput demands imposed by the robotic arm. Additionally, the non-linear response of the TECP RH instrument at the low RH expected during the daytime hours introduced uncertainties (Zent, et al., 2010). While the data has been adjusted via recalibration twice since 2009, (Zent et al., 2016; and Fischer et al.,2019), the relative humidity sensor did not consistently capture data during many of the recorded dust devil events. To date, PML and the Mars Science Laboratory (MSL) missions are the only surface probes that have provided *in situ* relative humidity measurements. The method used in this thesis allows relative humidity estimation, with reasonable certainty, based on given surface conditions.

2.1 Mars Water Vapor Content and Pressure Relaxation

Zuckerwar and Meredith (1984) demonstrated the significant degree to which relative humidity influenced frequency-dependent sound attenuation in air. When those acoustic parameters are employed to estimate terrestrial pressure relaxation coefficients, variations in relative humidity at typical diurnal temperatures produce larger variations in pressure relaxation coefficient than ambient temperature variations. Even though the molar concentration of atmospheric water vapor is extremely small on Mars, due to its low ambient temperatures and pressures the atmosphere can be quite humid, producing water ice condensation clouds,

confirmed as early as 1973 via Mariner 9 infrared imagery (Curran, et al., 1973). Water-derived clouds have been observed and studied since that time.

The knowledge that H_2O can strongly impact the relaxation of CO_2 together with the demonstrated effects of relative humidity on terrestrial η_p, was the scientific motivation for extracting reasonable relative humidity estimates for the ambient pressure and temperature environments in the vicinity of each observed dust devil event. In this work, *Volume Mixing Ratios* for water vapor have been utilized in conjunction with seasonal water column data collected by the Mars Global Surveyor Thermal Emission Spectrometer (MGS TES), (Smith, 2002), to estimate the local relative humidity .

Together with thermophysical properties, the relative humidity can be utilized subsequently to estimate η_p for each observed dust devil encounter. Having a simple method for determining local relative humidity should be useful for future scientific studies of the Martian atmosphere in general. Seasonal relative humidity levels also provide insight regarding relaxation influences due to the small molar quantities of H_2O present in Mars's atmosphere.

CHAPTER 3

MARTIAN ACOUSTIC AND NON-EQUILIBRIUM PROPERTY MODELS

The non-equilibrium dust devil model described in Section 1.2, can enable forensic assessment utilizing orbital dust devil observations of the width of the scoured ground track and associated funnel cloud height estimates. Following application of this model to terrestrial events, if the surface temperature, pressure, and relative humidity associated with a dust devil observation can be inferred, the maximum swirl velocity and minimum pressure characterizing that dust devil can be estimated. Those estimates are crucial for establishing surface structural design guidelines for deployed solar arrays and other fixed-base structures. However, the proposed approach is only feasible if reliable Mars-atmosphere-derived pressure relaxation coefficients and associated dust devil turbulent eddy viscosity ratios can be developed. Before turbulent influences can be addressed, it is necessary to develop pressure relaxation coefficient estimates.

An updated Mars atmospheric model was needed. In addition to relative humidity, the thermophysical properties needed for the application of the Ash and Zardadkhan model are saturated water vapor pressure (for solid-vapor phase transitions at Martian ambient conditions), specific heat, dynamic viscosity, and local density. Acoustic relaxation strength and relaxation time estimates for Martian atmosphere were also needed. Temperatures near the Martian surface can range from 140 K to 310 K, with the coldest temperatures occurring in the polar regions during winter (Catling, 2014). Temperature-based property tables for the various molecular species do not span, typically, the applicable temperature range. For convenience, MATLAB scripts were written to generate first principle-based tables spanning the required daytime temperature range from 180 K to 300 K. The first principles basis for the Martian atmosphere follows. Table 3 spans the temperature range for the four dust devils cataloged in Table 2; complete tables are contained in Appendix A.

Temp K	**p_{sat}/p_r** (over ice)	**c_p CO_2**	**c_v CO_2**	**c_p^0** Mars atm.	**C_v^0** Mars atm.	**C_{vib}**	**c_p^∞**	**c_v^∞**	**μ** Mars atm.	**$P*\tau_{VT}$**
227	0.0379233	762.583	573.663	764.248	573.008	101.363	666.30	475.06	1.154E-05	0.02429
228	0.0427087	763.634	574.714	765.263	574.023	102.414	666.30	475.06	1.159E-05	0.02484
229	0.0480483	764.683	575.763	766.277	575.037	103.463	666.30	475.06	1.164E-05	0.0254
230	0.0540004	765.731	576.811	767.289	576.049	104.511	666.30	475.06	1.169E-05	0.02596
231	0.0606285	766.777	577.857	768.300	577.060	105.557	666.30	475.06	1.174E-05	0.02654
232	0.0680026	767.822	578.902	769.310	578.070	106.602	666.30	475.06	1.179E-05	0.02712
233	0.0761986	768.865	579.945	770.318	579.078	107.645	666.30	475.06	1.185E-05	0.02771
234	0.0852996	769.907	580.987	771.324	580.084	108.687	666.30	475.06	1.19E-05	0.02832
235	0.0953962	770.946	582.026	772.329	581.089	109.726	666.30	475.06	1.195E-05	0.02893
236	0.1065869	771.984	583.064	773.332	582.092	110.764	666.30	475.06	1.2E-05	0.02955
237	0.1189791	773.020	584.100	774.333	583.093	111.800	666.30	475.06	1.205E-05	0.03019
238	0.1326896	774.054	585.134	775.332	584.092	112.834	666.30	475.06	1.21E-05	0.03083
239	0.1478451	775.086	586.166	776.329	585.089	113.866	666.30	475.06	1.215E-05	0.03148
240	0.1645833	776.116	587.196	777.324	586.084	114.896	666.30	475.06	1.22E-05	0.03215

Table 3: Excerpt of MATLAB generated thermophysical properties for a range of 225 – 240 Kelvin and 0.03% atmospheric conc. Of H_2O.

3.1 Mars Atmospheric Composition

The atmosphere of Mars is predominately CO_2, and a 100% CO_2 atmosphere approximation has been common. However, the present model considers species-related acoustical attenuation and relaxation effects when determining volume viscosity and associated non-equilibrium parameters to include relative humidity in the η_p estimates. This study includes H_2O, as well as all elemental gases present in greater concentrations than H_2O. The commonly accepted globally averaged mole-percent based distribution is summarized in Table 4.

Gas	Mole-based % contribution
CO_2	95.32%
N_2	2.7%
Ar	1.6%
O_2	0.13%
CO	0.08%
H_2O	0.03% (variable)

Table 4: Mars atmospheric model (Barlow, 2008).

Unlike Earth, pole-to-pole transport of atmospheric carbon dioxide resulting from a seasonal condensation-sublimation cycle produces significant variations in local surface density and pressure. Seasonal density variations influence the composition of the atmosphere. Based on three Mars years of data collected by the Sample Analysis at Mars (SAM) instrument onboard the Curiosity rover in Gale Crater (near the equator), an annual average atmospheric composition profile was developed. Those data were generally in good agreement with already established profiles (Trainer et al., 2019). The annually averaged seasonal fluctuations in N_2, Ar, O_2, and CO are summarized in Table 5.

Atmospheric Component	Annual Mean Mixing Ratio	Uncertainty of mean	Seasonal variation from mean	Approximate measurement error
CO_2	0.951	±0.003	1 %	2.9 %
N_2	0.0259	±0.0006	10 %	3.2 %
Ar	0.0194	±0.0004	9.7 %	2.0 %
O_2	0.00161	$\pm 9x10^{-5}$	13 %	18 %
CO	0.00058	$\pm 8x10^{-5}$	36 %	6.1 %

Table 5: Annual mean volume mixing ratios for Mars atmosphere (Trainer, M.G., et al, 2019).

Trainer et al. observed that all but O_2 appear to follow the expected seasonal pole to pole transport of carbon dioxide. The O_2 seasonal variation lagged slightly behind, peaking in Summer and Fall, and CO_2 experienced peak seasonal variation in Spring and Winter (Trainer et al., 2019). Even though the Trainer study was unable to fully account for the unexpected fluctuations in oxygen and despite the large measurement error, it was necessary to consider the seasonal variations of the atmospheric components here and whether this affected the present calculations. A quick comparison between the Gale Crater study mean mixing ratios and the model employed represented only a 0.027% difference in molar mass fraction for Mars atmosphere. At the peak seasonal variation from the mean, the difference is 0.4% and has no influence on relative humidity calculations. For purposes of this study, other than water vapor fractions, the Mars reference atmospheric composition in Table 4 (Barlow, 2008) is appropriate.

The average H_2O concentration for the Martian atmosphere is nominally 0.03% (variable), and that variation is seasonal and latitudinal. The dust devil events reported in Table 2 occurred during Sols 90, 95, 118, and 136, which were during the summer season at or near 68°N latitude. At this time and latitude, the maximum precipitable water[3] available in the atmosphere can range typically from 40 to 70 *pr-μm* vs the annual average of 10-20 *pr-μm* corresponding to the average value of 0.03% H_2O atmospheric concentration (Trokhimovskiy et al., 2015; Smith, 2002). Sols 90 and 95, according to the Smith TES data (shown in section 4.5, Figure 1), corresponded with approximately 65 and 60 pr-μm of water, respectively while Sols 118 and 136 corresponded to water vapor column values closer to 50 and 45 pr-μm respectively. Thus, this work has assumed an H_2O concentration of 0.12 % for Sols 90 and 95 and 0.08 % for Sols 118 and 136 as reasonable estimates of local H_2O concentrations in the atmosphere.

The molar mass of Mars atmosphere, M_{Matm}, and Mars dry atmosphere, $M_{dry\ Matm}$, are determined by summing the products of the molar mass and mole fraction of the individual components of the mixture giving: $M_{Matm} = 43.44\ g/mol$ and $M_{dry\,Matm} = 43.40\ g/mol$.

Using $R_{gas} = \frac{R_u}{M_{gas}}$, where R_u is the universal gas constant,

$$R_{dry\ Matm} = 191.54\ {}^{Pa\,m^3}/_{kg\,K},$$

[3] The maximum precipitable water available in the atmosphere, given in *pr-μm*, is the depth of liquid water in a column of atmosphere, if all of the water were precipitated as rain.

$R_{Matm} = 191.5\ {}^{Pa\,m^3}/_{kg\,K}$ for 0.03% concentration of H_2O,

$R_{Matm} = 191.47\ {}^{Pa\,m^3}/_{kg\,K}$ for 0.08% concentration of H_2O,

and $R_{Matm} = 191.44\ {}^{Pa\,m^3}/_{kg\,K}$ for 0.12%.

Based on these estimates, the density of Mars atmosphere at the ambient conditions associated with each dust devil event can be computed employing $\rho_\infty = \frac{P_\infty}{R_{matm} T_\infty}$.

3.2 Saturation Vapor Pressure

The saturated vapor pressures for calculating maximum water vapor molar concentrations and local relative humidity in Mars atmosphere were required. There have been many predictions utilizing the Clapeyron Equation over the years. Murphy and Koop (2005) compared the accuracy of several of these, and while many of the derivations have merit, the Goff and Gratch, (1946) classical formulation remains the most accurate determination of saturated vapor pressure variation with temperature. Goff made minor corrections to the original formulation in 1965 (Goff, 1965), and the corrected formulation was employed to produce the tabulated property data. Note that the values for p_{ice} will, in most cases, be the relevant P_{sat} for Mars conditions. The Goff equation is:

$$\log\left(\frac{p_{ice}}{p_r}\right) = \log(611.657) - 9.096936\left(\frac{T_t}{T} - 1\right) - 3.56654\log\left(\frac{T_t}{T}\right) + 0.876817\left(1 - \frac{T_t}{T}\right) \quad (3.1)$$

$$\log\left(\frac{p_{liq}}{p_r}\right) = \log(611.657) + 10.79586\left(1 - \frac{T_t}{T}\right) - 5.02808\log\left(\frac{T}{T_t}\right) + 1.50474 \times 10^{-4}\left(1 - 10^{-8.29692\left(\frac{T}{T_t} - 1\right)}\right) + 0.42873 \times 10^{-3}\left(10^{4.76955\left(1 - \frac{T_t}{T}\right)} - 1\right). \quad (3.2)$$

3.3 Specific Heats

The principal component of the variational approach is the pressure relaxation coefficient, and the subsequent relations for relaxation times, relaxation strength, and volumetric viscosity require specific heats. Specific heat formulations can vary based on conditions and the degree to

which all the molecular states, or degrees of freedom, are excited. The terms $c_p^0 \; and \; c_v^0$ represent the total, or unfrozen isobaric and isochoric specific heats, where vibrational contributions are included; $c_p^\infty \; and \; c_v^\infty$ refer to the frozen specific heats, which do not include any vibrational contributions.

Argon atoms can only contribute translational energy to specific heat. Diatomic N_2, O_2, and CO molecules each have three translational and two rotational contributions, while their vibrational contributions are only accessible at much higher temperatures than Martian surface conditions and have therefore been neglected. The dominant CO_2 molecules have three translational, two rotational, and a maximum of three vibrational degrees of freedom. Again, due to the low temperatures encountered in the Martian atmosphere, only the double-degenerate bending mode of CO_2, with a vibrational temperature, θ_{vib}, of 960 K, is likely to affect Mars atmospheric departures from equilibrium conditions (Bass and Chambers, 2001). This makes CO_2 the only temperature dependent specific heat contributor to Martian atmosphere over the expected range of temperatures. The unfrozen constant pressure specific heat for CO_2 is calculated using (D. Bücker et al., 2003):

$$c_p^0 = \frac{5}{2} R_{CO_2} + c_{p,rot}^0 + R_{CO_2} \sum_{i=1}^{N_{vib}} \left(\frac{\theta_{vib,i}}{T} \right)^2 \frac{e^{\theta_{vib,i}/T}}{[e^{\theta_{vib,i}/T} - 1]^2} \tag{3.3}$$

where,

$$c_{p,rot}^0 = R_{CO_2}, \;\; N_{vib} = 2, and \; \theta_{vib} = 960 \; K.$$

The frozen constant pressure specific heat for CO_2 is:

$$c_p^\infty = \frac{5}{2} R_{CO_2} + \frac{2}{2} R_{CO_2} = \frac{7}{2} R_{CO_2}. \tag{3.4}$$

To a good approximation, c_p for H_2O can be considered independent of temperature at Mars ambient surface conditions (Rogers and Mayhew, 1995). For nominal Mars conditions, the constant pressure specific heat of water vapor is taken as 1853 J/kg-K. The constant pressure

specific heats for each species, based on their molecular weights have been employed for all calculated specific heats. The frozen and unfrozen specific heats at constant pressure for the remaining gases are presented in Table 6.

Gas	$\boldsymbol{c_p^{\infty} = c_p^0}$
Ar	$\frac{5}{2} R_{Ar}$
N_2	$\frac{7}{2} R_{N_2}$
O_2	$\frac{7}{2} R_{NO_2}$
CO	$\frac{7}{2} R_{CO}$

Table 6: Specific heats for remaining atmospheric gases.

It follows that, $c_{p,mars}^0 = \sum w_{gas} * c_{p,gas}^0$ and $c_{p,mars}^{\infty} = \sum w_{gas} * c_{p,gas}^{\infty}$, where $w_{gas} = molar\ mass\ fraction\ of\ the\ gas.$ Using the relation $c_v = c_p - R_{gas}$, the frozen and unfrozen specific heats at constant volume are thusly known.

3.4 Dynamic Viscosity

Dynamic viscosities were calculated based on species concentrations over the range of temperatures utilizing Sutherland's formula (Sutherland, 1893),

$$\mu = \mu_0 \frac{T_0 + C_n}{T + C_n} \left[\frac{T}{T_0}\right]^{3/2}. \tag{3.5}$$

The constants, C_n, for each species were taken from (Crane Company, 1988), the reference viscosities, μ_0, and reference temperatures, T_0 from *CRC Handbook of Chemistry and Physics* (CRC,1984) and are given in Table 7.

Gas	C_n **[K]**	T_0 **[K]**	μ_0 **[μPa s]**
Ar	144.4	273.15	21.25
N_2	111	300.55	17.81
O_2	127	292.25	20.18
CO_2	240	293.15	14.8
CO	118	288.15	17.2

Table 7. Sutherland constants with reference temps and viscosities (CRC, 1984).

The water ice-vapor phase transition conditions at the low temperatures encountered on Mars required a different viscosity correlation. The relation (J.F. Crifo,1989)

$$\mu_{H_2O} = 9.25\ x\ 10^{-5}\left(\frac{T}{300}\right)^{1.1}, \tag{3.6}$$

was employed.

Due to differences in the molecular weights of each atmospheric species, the sum of partial viscosities was estimated utilizing a weighted (by the square root of the molecular weight of each species) average (Davidson, 1993). When the molecular weights are not similar, a simple summation of the products of viscosity and their molecular weights is not accurate. In the absence of large proportions of hydrogen, the Herning and Zipperer (1936) equation is justified, when there are no large discrepancies between the reference viscosities of the lesser components compared with the main component of the mixture. The molecular weight-based viscosity equation given by Herning and Zipperer is:

$$\mu_{mix} = \frac{\sum(\mu_i X_i \sqrt{M_i})}{\sum(X_i \sqrt{M_i})}. \tag{3.7}$$

3.5 Relative Humidity

Relative humidity at a given temperature is defined as the ratio of the partial pressure of water vapor present to its saturated vapor pressure in the atmosphere mixture. On Earth it is easily determined via dew point temperatures, a readily available parameter common in weather monitoring and forecasting. Relative humidity can also be determined using meteorological specific humidity ratios for water vapor in a gaseous mixture with the relative humidity relation:

$$RH = \frac{q}{q_s}, \tag{3.8}$$

where q is the specific humidity[4], and q_S is the saturation specific humidity. The ratio of the mass of water vapor to the mass of Mars atmosphere describes q as:

$$q = \frac{m_{water\ vapor}}{m_{matm}}. \tag{3.9}$$

Starting with the Viking lander missions in 1976, near surface and overall atmospheric water vapor content has been an important focus of study. Through the compilation and comparison of data from missions and experiments from Viking 1 and 2, Mars Global Surveyor, Mars Reconnaissance Orbiter, and Mars Express, a great deal is now known concerning the annual and diurnal variations of water vapor in Mars's atmosphere. Based on this knowledge, global seasonal moisture patterns have been established and can be utilized to estimate moisture distributions in the absence of in situ data. While there are small variations from year to year, the seasonal cycles are consistent and repeatable (Trokhimovskiy et al., 2015) and, therefore, are reasonable estimators when employed to estimate relative humidity.

[4] Specific humidity is equivalent to the engineering definition of humidity ratio.

Michael Smith of NASA Goddard Space Flight Center processed the data collected from the Mars Global Surveyor Thermal Emission Spectrometer (MGS TES) over one Martian year and provided a detailed analysis of the global seasonal cycle of water vapor abundance (Smith, 2002). His seasonal global water vapor column abundance, given in precipitable microns, and associated condensation height assessments have been employed in this study to estimate near surface relative humidity. Seasonal water column abundance and water condensation altitudes are displayed as functions of latitude and the associated areocentric longitude of the Sun (L_s) in Figures 2 and 3.

To translate the humidity ratio into a more useful form, the numerator and denominator of the mass mixing ratio can be interpreted on a per unit volume (per m^3) basis to yield a ratio of the water vapor density to the density of dry atmosphere. After utilizing the ideal gas law, the Volume Mixing Ratio (VMR), can be expressed (Stull, 2015) in kg/kg as:

$$VMR = \frac{\varepsilon \cdot p_{vap}}{P - p_{vap}(1-\varepsilon)} \ , \tag{3.10}$$

where $\varepsilon = \frac{R_{dry\ matm}}{R_{water\ vap}} = 0.4149$. The saturated water vapor condition is obtained by replacing the vapor pressure, p_{vap}, with the saturated vapor pressure at the specific temperature. This yields the saturated volume mixing ratio, or the saturation specific humidity:

$$VMR_{sat} = \frac{\varepsilon \cdot p_{sat}}{P - p_{sat}(1-\varepsilon)} \ . \tag{3.11}$$

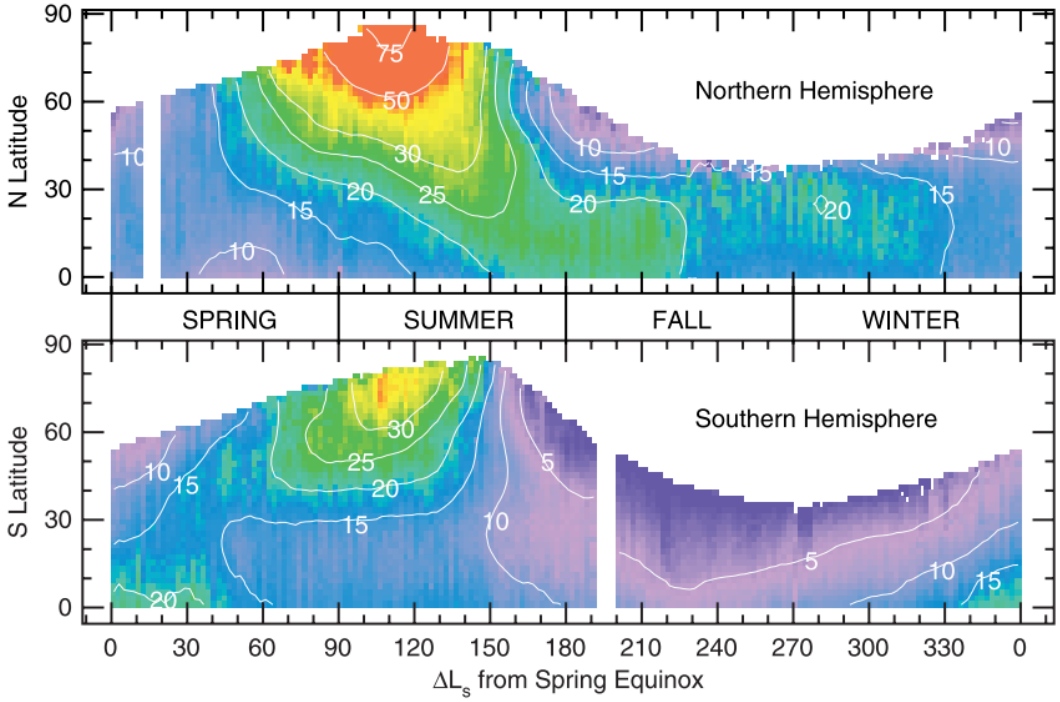

Figure 2. Water column abundance in precipitable microns, pr-μm (Smith, 2002).

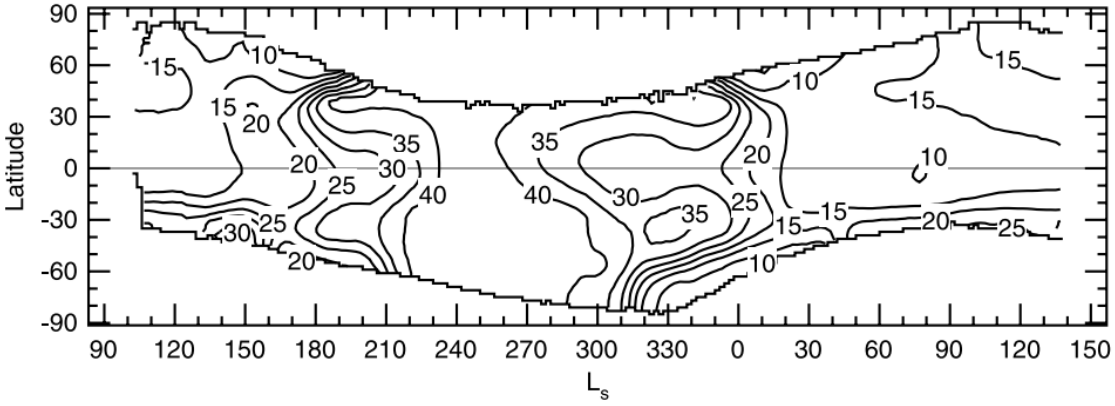

Figure 3: Water condensation levels, in kilometers above the surface (Smith, 2002).

Saturation pressures have been calculated and can be used to determine VMR_{sat} using relation (3.10), but the expression for *VMR* requires additional refinement in order to relate it to precipitable water column data (Smith, 2002).

A mole-fraction-based volume mixing ratio for specific humidity can be defined as the ratio of the number of moles of water vapor to the number of moles of Mars dry atmosphere per unit volume, denoted by the subscript *Matm*. In this case, the number of water vapor molecules per m^2 in an atmospheric column is divided by the total number of molecules per m^2 of Mars dry atmosphere in the same column. Then, Eq. (3.10) can be written:

$$VMR = \frac{n_{vap}}{n_{Matm}}. \tag{3.12}$$

The number of molecules can be calculated by dividing the mass per m^2 by the mass of a single molecule giving:

$$n_{vap} = \frac{m_{vap}}{M_{vap} \times 1.661 \times 10^{-27}} \quad and \tag{3.13}$$

$$n_{matm} = \frac{m_{Matm}}{M_{Matm} \times 1.661 \times 10^{-27}}\ . \tag{3.14}$$

Since the water column abundance, H_2O_{column}, compiled in precipitable microns, represents the liquid water equivalent in micrometers and the nominal density of liquid phase water is 1000 kg/m^3, m_{vap} can be determined from the precipitable water column data (Smith, 2002):

$$m_{vap} = H_2O_{column} \times 0.001 \frac{kg}{m^2}. \tag{3.15}$$

Assuming hydrostatic equilibrium and local concentrations of water vapor are well mixed in the atmospheric column, the mass of dry atmosphere is equal to the pressure difference between two heights in the atmosphere divided by the gravitational constant (3.74 m/s^2 on Mars). The pressure near the bottom of the water column is known, and the pressure at the top of the water column can be assumed to be equal to the pressure at the condensation height. From Figure 2, the condensation height is known. Utilizing the barometric pressure approximation from the

barometric formula for an adiabatic atmosphere, the pressure at the condensation height is thusly known.

This barometric formula utilizes an ideal gas model relating pressure and absolute temperature through a dry adiabatic temperature lapse rate. Treating the Martian atmosphere as an ideal gas and gravity as a constant, the expression for P at the top of the water column, or its condensation height, is obtained through the integration of

$$dp = \frac{-g}{R_{matm}\,T(z)}\,p\,dz, \tag{3.16}$$

where z is the height. $T(z) = T_{surf} + \alpha z$, with the lapse rate, $\alpha = \frac{-g}{c_p}$, found using g = 3.74 m/s^2 and c_p at T_{surf}. After integration, the expression for P at the top of the water column becomes (Lente and Ősz, 2020):

$$P_{top} = P_{surf}\left(1 - \frac{\alpha}{T_{surf}}z\right)^{\frac{-g}{R_{matm}\,\alpha}}. \tag{3.17}$$

Now, having the mass of dry atmosphere, n_{matm} is known. Mathematically, the units cancel in VMR (molecules per m^2 / molecules per m^2) and in VMR_{sat} (kg/kg), enabling equations (3.11) and (3.12) to be employed for estimating relative humidity at a specified temperature, pressure, latitude, and Solar longitude as:

$$RH = \frac{VMR}{VMR_{sat}}. \tag{3.18}$$

At night, depending on season and location, the relative humidity can vary between 20% and supersaturation [(Pal et al, 2019), (Fischer et al, 2019), (Martínez et al.,2017)]. All three studies concluded the daytime RH values are generally less than 5% between the hours of 10:00 and 18:00 LMST based on data from the PHX and MSL surface measurements. This generality is due primarily to sensor accuracy limitations (±5% for PHX and ±8% for MSL, Martínez, et al., 2017), which creates uncertainty in the estimated values employed for verification. However,

their data could still be used as a qualitative judge of the reasonableness of the present surface RH estimates.

In terrestrial applications, it is standard practice to calculate RH using the saturated vapor pressure for liquid water (ANSI-ASA S1.26-2014) even at cold temperatures; however, for Mars atmospheric conditions, the calculation of RH using vapor pressures for water ice is more appropriate (Rivera-Valentín et al., 2018). The average atmospheric pressure is just below the triple point for H_2O, which is ~612 Pa at 273 K. The range of temperatures and pressures at Mars severely limit the possibility of H_2O being present in liquid form. Examining the extremes

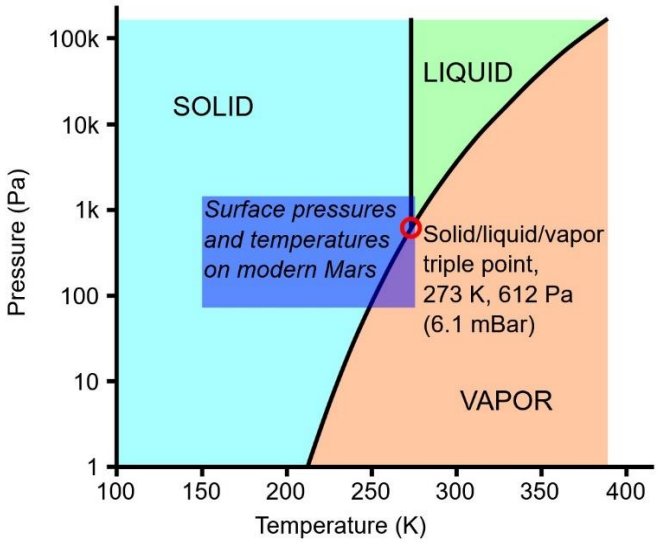

Figure 4: Phase diagram superimposed with the approx. surface conditions of Mars (D. Hobley, 2012).

finds the lowest pressures, around 70 Pa, at the top of Olympus Mons and the highest, around 1400 Pa, at the bottom of Hellas Crater (Carr, 2006). The temperatures can only rarely be as high as 310 K (Catling, 2014) but would have to be accompanied by a higher-than-average

surface pressure. If this were to occur, it would be only for a brief time in the middle of the day, which also happens to be the driest part of the day. For this reason, the two missions (MSL, and PHX) that included RH sensors were calibrated for RH with respect to ice (Rivera-Valentín et al., 2018).

Figure 5 shows temperature and RH measurements from PHX and MSL landing sites (Fischer et al., 2019) referenced to ice-vapor phase transitions, RH_{ice} data, that have been converted to the higher liquid-vapor phase transition pressures, RH_{liq}, in order to be consistent with terrestrial interpretation. Looking at this data and keeping in mind that the general statement of < 5% refers to RH_{ice}, the general trend for warmer temperatures, >235 K, is certainly 5% or less, but for lower daytime temperatures as for the events on Sols 118 and 136, RH_{liq} measurements exceeding 5% were recorded.

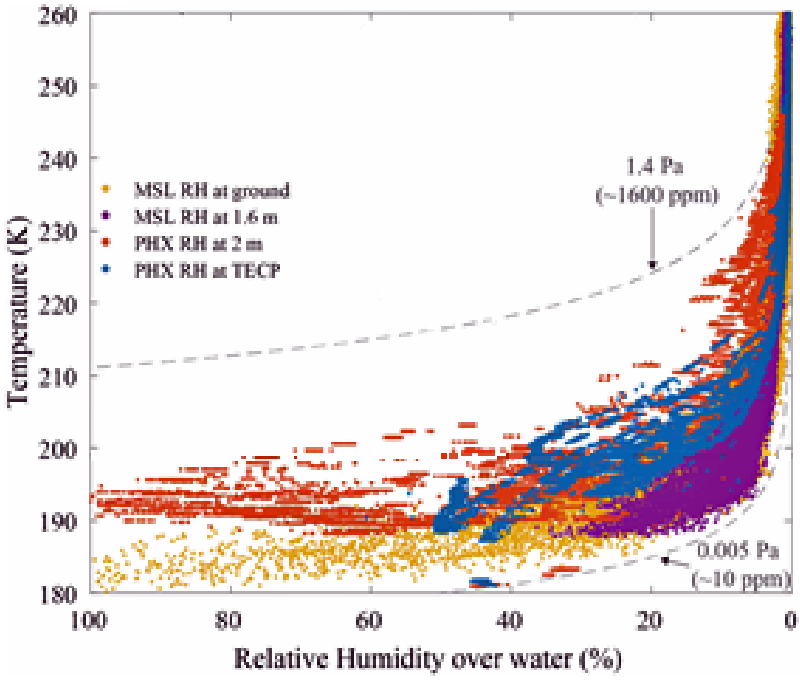

Figure 5. Temp and relative humidity over liquid water with min and max TECP measured vapor pressures (Fischer, et al., 2019).

For ease of comparison with Figure 5, the volume mixing ratio relations just described were calculated with saturated vapor pressures over liquid water and water ice giving both RH_{liq} and RH_{ice} values for the observed dust devil encounters. Table 8 summarizes the calculated RH values, along with the ambient density for each dust devil observation. The comparison shows that the relative humidity estimates for the four Phoenix dust devil data sets are consistent with

Sol	**$\Delta P_{C/L}$**	**T^{∞}**	**P^{∞}**	**ρ_{∞}**	**RH_{ice}**	**RH_{liq}**
90	2.58	240	765.4	0.0167	1.84	1.29
95	3.56	240	752.5	0.0164	1.69	1.18
118	2.37	228	739.5	0.0169	6.19	3.95
136	2.51	227	727	0.0167	6.67	4.22

Table 8. Calculated relative humidity and density for each Phoenix dust devil.

expected daytime RH_{liq} values. Accepting that the low pressure and low temperature environment makes the formation of liquid water nearly impossible (Haberle et al., 2001), all remaining calculations in this work utilize RH_{ice}.

3.6 Acoustical Properties

Acoustics, as a science discipline, studies the propagation and attenuation of sound, or pressure waves, in fluids. The two dissipative parameters η_v and η_p, resulting from the work of Zuckerwar and Ash (2006, 2009) for inclusion of non-equilibrium effects in their viscous fluid model, are elements of classical theory based on the absorption of sound. From Kinetic Molecular Theory, the rates at which molecular components of a gas mixture transfer energy can be employed to determine the frequency-dependent reaction times among the molecules making up Martian atmosphere (Schwartz, Slawsky, & Herzfeld, 1952). Those interactions can be

precisely described by their relationship to the relaxation rates of the fluid. To utilize the model equations in section 1.2, η_p is needed and was formulated by Zuckerwar and Ash (2006) as

$$\eta_p = \tau_{VS}, \tag{3.19}$$

where, in this case, τ_{VS} is the constant volume relaxation time of Mars's atmosphere and is classically expressed (Herzfeld and Rice, 1928) as

$$\tau_{VS} = \frac{c_p^{\infty}}{c_p^{0}} \cdot \tau_{VT} \, . \tag{3.20}$$

As discussed in section 3.3, CO_2 is considered here to be the only component capable of making a vibrational contribution to the energy transfer process. Thus, simplifying the determination of the relaxation properties by employing a single energy transfer reaction. The relaxation time at constant volume and temperature for a single reaction process is expressed in seconds as:

$$\tau_{VT} = \frac{1}{k - k_b} \, , \tag{3.21}$$

where *k*, and k_b are the forward and reverse rates of reaction respectively and through the principle of detailed balance *k* and k_b are related by:

$$k_b = k \, e^{-\theta_j / T} \, , \tag{3.22}$$

where θ_j is the vibrational temperature. The rate, k, at which CO_2 will transfer vibrational energy in the atmosphere is the sum of the mole fractions multiplied by the transfer rates of energy from CO_2 to each component of the atmosphere:

$$k = X_{CO_2} k_{CO_2} + X_{N_2} k_{N_2} + X_{Ar} k_{AR} + X_{O_2} k_{O_2} + X_{CO} k_{CO} + X_{H_2O} k_{H_2O}. \tag{3.23}$$

The relaxation paths for CO_2 through its bending mode, in collisions with N_2 and H_2O are well understood at temperatures from 300 K to 600K through experimentation by Shields, Warf, and Bass (1973). Collisions between the other atmospheric components are not as well understood, but theory suggests it is reasonable to assume that $k_{N2} = k_{Ar} = k_{CO} = k_{O2}$, since their contributions to the atmospheric mixture are small and their molecular structures are similar (Bass and Chambers, 2001). From the extensive Landau and Teller (1936) consideration of molecular collisions, we understand the temperature dependence of energy transition probabilities and how the rate constant is related to the transition probability through the collision frequency, $f_c = 1.25P/\mu$, where P is pressure and μ is dynamic viscosity. Shields, Warf, and Bass (1973) applied this approximation to their experimental results showing

$$k_{CO_2} = 0.219 \left(\frac{P}{\mu}\right) e^{\left(\frac{-60.75}{T^{\frac{1}{3}}}\right)}. \tag{3.24}$$

Similarly, the rate constant formula for nitrogen was determined and subsequentially the rate constants for argon, oxygen, and carbon monoxide are assumed expressed as:

$$k_{N_2} = k_{Ar} = k_{O_2} = k_{CO} = 1.44 \left(\frac{P}{\mu}\right) e^{\left(\frac{-78.29}{T^{\frac{1}{3}}}\right)}. \tag{3.25}$$

Through measurement, Lewis and Lee (1965) determined the relaxation of CO_2 by H_2O to be temperature independent; thus, the rate constant can be represented:

$$k_{H_2O} = 6 \times 10^{-2} \left(\frac{P}{\mu}\right). \tag{3.26}$$

Working with a single energy-transfer process, assuming a nominally isentropic flow, the resulting acoustic equation of state provides two expressions for the relaxation strength (H.J. Bauer, 1965; J. Lamb, 1965), S, as

$$S = 1 - \frac{\tau_{VS}}{\tau_{PS}} \,, \tag{3.27}$$

where τ_{PS} is the isentropic relaxation time at constant pressure, or when contributions to specific heat capacity are known,

$$S = \frac{R_{mair} c_{vib}}{c_v^0 c_P^\infty} \,. \tag{3.28}$$

c_{vib} is the vibrational contribution to the specific heat capacity given by Einstein's formula (Atkins, de Paula, and Keeler, 2018),

$$c_{vib} = \sum_{i=1}^{N_{vib}} \left(\frac{\theta_{vib,i}}{T}\right)^2 \frac{e^{\theta_{vib,i}/T}}{[e^{\theta_{vib,i}/T} - 1]^2} \,. \tag{3.29}$$

CHAPTER 4

PRESSURE RELAXATION ESTIMATES AND BULK VISCOSITY

V. O. Knudsen (1931) proved that relative humidity has a significant influence on the absorption of sound in the terrestrial atmosphere. Zuckerwar and Meredith (1984) verified this experimentally at low frequencies from 10 to 2500 Hz, and Harris (1967) covered the frequency interval of 2000 to 12500 Hz. As the relative humidity increases, the spectral rate of absorption decreases. That effect was interpreted in terms of bulk viscosity and pressure nonequilibrium by Zuckerwar and Ash (2006, 2009) who demonstrated that increases in relative humidity enabled the atmosphere to respond to high frequency pressure fluctuations more efficiently. The saturation water vapor content (100% RH) for Mars's atmosphere represents an extremely small mole fraction. However, experimental data related to the possible influence of humidity on pressure relaxation of a 95% carbon dioxide atmosphere at Mars' surface conditions is lacking.

Zuckerwar developed the method used here for estimating the pressure relaxation coefficient, η_p, based on a mole-fraction weighted average applied to the relaxing specific heats. Using the method outlined in the American National Standard S1.26-2014 for the conversion of RH data to the mole fraction of water vapor, x_h, the normalized total, or unfrozen, specific heats can be written:

$$c_p^0 = c_p^\infty + (1 - x_h) c_{vib} \cdot w_{CO_2} \tag{4.1}$$

and

$$c_v^0 = c_v^\infty + (1 - x_h) c_{vib} \cdot w_{CO_2}, \tag{4.2}$$

where w_{CO_2} is the mass fraction of CO_2, i.e., the component subjected to vibrational relaxation. Additionally, the relative humidity weighted relaxation strength is defined as:

$$S = \frac{R_{matm}(1 - x_h) c_{vib}}{c_v^0 c_P^\infty} . \tag{4.3}$$

The four documented dust devils encountered by the Phoenix lander have been examined in terms of nonequilibrium and bulk viscosity parameters. Table 9 summarizes estimates of x_h based on the calculated RH and specified temperatures. The volume, or bulk viscosity, η_V, from the variational approach of Zuckerwar and Ash (2006) is

$$\eta_V = \tau_{PS}\left(\frac{P^{\infty}}{\gamma}\right), \qquad where \;\; \gamma = \frac{c_p^0}{c_v^0}, \tag{4.4}$$

and recalling equations (3.19) through (3.21), the pressure relaxation coefficient can be expressed as

$$\eta_p \;=\; \tau_{VS} = \frac{c_p^{\infty}}{c_p^0} \cdot \tau_{VT}\,. \tag{4.5}$$

	Sol 90 [240 K]	**Sol 95** [240 K]	**Sol 118** [228 K]	**Sol 136** [227 K]
RH	~ 2%	~ 2%	~ 6%	~ 7%
$\mathbf{x_h}$	0.0026	0.0027	0.0021	0.0028
$\boldsymbol{\eta_p}$ (μs)	36.02	36.64	29.10	29.01
$\boldsymbol{\eta_v}$ (Pa s)	0.0220	0.0220	0.0170	0.0167

Table 9. Relative humidity, mole fractions of water vapor, and acoustically based estimates of η_p & η_v.

Bulk viscosity is a property that cannot be measured directly; however, it can be derived from other measurable quantities such as the sound absorption coefficient, α (Jaeger, Matar, and Müller, 2018). Tisza (1942) was the first to include bulk viscosity in sound absorption calculations, and his derivation identified a strong relationship with relaxation times based on molecular degrees of freedom. Bass and Chambers (2001) considered the absorption of sound in

the Martian atmosphere using the simplified atmospheric composition model of 95.3% CO_2, 2.7% N_2, 1.6% Ar, and variable amount of H_2O (0% and 1%). The absorption coefficients calculated with bulk viscosity and pressure relaxation coefficients estimated in this work should be similar to the Bass and Chambers estimates.

Based on the CO_2 dominance of Mars's atmosphere, vibrational relaxation is the dominant process (H.O. Knesser, 1965) and is used here for the comparison. Using the expression for a_{vib} (H.E. Bass, et al., 1984)

$$a_{vib} = \frac{\left(\pi S/c\right)\left(f^2/f_r\right)}{\left[1+\left(f/f_r\right)^2\right]}\,, \tag{4.6}$$

where the speed of sound is , $c = \left(\gamma \frac{RT}{M}\right)^{1/2}$, the relaxation strength, S, from relation (3.26), and the relaxation frequency is, $f_r = 1/(2\pi\tau_{VS})$. Noting the frequency dependence of τ_{VS}, or η_p , Table 10 compares the present results with Bass and Chambers (2001), showing good agreement.

	Bass & Chambers (2001) (Np/m) at 500 Hz	This work (Np/m) at 500 Hz
a_{vib} at 200 K	0.03	0.02
a_{vib} at 300 K	0.1	0.15

Table 10: Vibrational absorption coefficient comparison.

On that basis, the acoustically based estimates for η_p and η_v appear to be reasonable for the more inclusive atmospheric model used in this work.

CHAPTER 5

MODEL APPLICATION AND RESULTS

With these variable definitions and estimates the non-equilibrium dust devil model from section 1.2 can be applied. Recalling from section 3.6 that the two non-equilibrium parameters, η_v and η_p, are elements of acoustical theory, the relaxation times and strength can be determined by making use of equations (3.18) through (3.20), along with the tabulated temperature dependent Mars thermophysical properties, and the RH normalized relations from equations (4.1) through (4.3). These quantities enable estimation of appropriate turbulent eddy viscosity, ν_{turb}, from Eq. (1.6), employing the known temperature and pressure characteristics of the four PHX dust devil events from Table 1. Since the work of Ash, Zardadkhan, and Zuckerwar (2011) yielded relations for the vortex characteristics of circulation, maximum swirl velocity, centerline angular velocity, circulation-based Reynolds number, and maximum height (see relations (1.2)-(1.5), (1.7), (1.8), and (1.9) in this work), these characteristics can now be estimated readily.

The relation for h_{max}, equation (1.8), requires a final adjustment in order to apply it to Mars dust devils. The Ash, Zardadkhan (2013) relation was a curve fit solution involving properties that were converted to Pa relative to sea level atmospheric pressure. A simple unit conversion of $\sqrt{\frac{610}{101325}}$ adjusts for that pressure influence, thereby making their correlation compatible with Mars thermophysical properties. Consequently, the terrestrial height estimate:

$$h_{max} = \frac{1.394}{\eta_p \omega}\sqrt{\frac{\nu}{\omega}}, \tag{1.8}$$

yields

$$h_{max,Mars} = \frac{0.1082}{\eta_p \omega}\sqrt{\frac{\nu}{\omega}}. \tag{5.1}$$

In the sections that follow, the results for the test cases of the PHX dust devils are examined and the reasonableness of the estimates discussed. Additionally, the usefulness of this method,

particularly in its application to past, future, in-situ, and remotely sensed orbital data will be further demonstrated.

5.1 Eddy Viscosity Ratios for Martian Dust Devils

Ash, Zardadkhan and Zuckerwar (2013) assumed the viscous inner core of a large-scale rotating atmospheric column was controlled by non-equilibrium pressure gradient forces in direct response to the coupling of centrifugal forces with unsustainable shearing strain rates near the rotational axis. Unlike the shearing discontinuity in the Rankine vortex model, the non-equilibrium structure produces plausible local stress gradients near the core. In short, on the basis that the rotating core is subject to non-equilibrium pressure forces and produces local Reynolds stress gradients at the interface between the inner and outer flow regions, Ash, Zardadkhan and Zuckerwar employed a simple eddy viscosity turbulence model:

$$\sigma_{ij} = (\mu + \mu_{turb})\left[\frac{\partial v_i}{\partial x_j} + \frac{\partial v_j}{\partial x_i}\right] = \rho \nu_{turb}\left[\frac{\partial v_i}{\partial x_j} + \frac{\partial v_j}{\partial x_i}\right]. \tag{5.2}$$

Subsequently, Ash and Zardadkhan (2021) have argued that the simple eddy viscosity model is fundamentally sound.

The terrestrial application of the eddy viscosity turbulence model was employed by Ash and Zardadkhan (2013) to predict physical properties of dust devils and tornadoes. Their results were in good agreement with observations from three detailed dust devil surveys in the Arizona Desert (Sinclair, 1973) and gave turbulent eddy viscosity to kinematic viscosity ratios of ${\nu_{turb}}/{\nu} = 3.2 \pm 1$. Employing dust devil measurements at Mars together with the estimated relaxation coefficients and densities, we have from relation (1.6), $\nu_{turb} = \eta_p \left({\Delta P_{c/l}}/{4\rho_\infty}\right)$. Dividing the tabulated temperature dependent dynamic viscosity by density, we now have the estimated turbulent viscosities and viscosity ratios for the four PHX dust devils, as summarized in Table 11. The sampling mean and standard deviation of the Mars ratios is ${\nu_{turb}}/{\nu} = 1.89 \pm 0.56$. The small standard deviation suggests that the turbulent viscosity to kinematic viscosity ratio can be considered a constant for Mars's atmosphere.

	Sol 90 [240 K]	**Sol 95** [240 K]	**Sol 118** [228 K]	**Sol 136** [227 K]
$\boldsymbol{\nu_{turb}}$ **(m^2/s)**	0.0014	0.0020	0.0010	0.0011
$\boldsymbol{\nu_{turb}/\nu}$	1.90	2.67	1.49	1.50

Table 11. Turbulent viscosity ratios for four PHX dust devils.

Due to the differences in atmospheric composition and ambient conditions, it is difficult to make direct comparisons with the terrestrial results for validation purposes. If we consider again the relation $\boldsymbol{\nu_{turb} = \eta_p \left(\frac{\Delta P}{4\rho_\infty}\right)}$, it is apparent that temperature dependent Martian density variations, account for significant differences compared with terrestrial sensitivities. While there is some pressure dependency in η_p , these values for Earth and Mars have similar magnitudes at similar temperatures. As the temperature difference appears to be the dominant (controlling) variable in this relation, a rough comparison can be made between hypothetical terrestrial and Martian dust devil events at a temperature of 240 K as in the Sol 90 PHX event. Choosing a typical Earth pressure drop of ~250 Pa (Sinclair, 1973) and for η_p at 240 K the estimate of ~24 μs is extrapolated via curve fit from Ash, Zardadkhan, and Zuckerwar (2011). Following the same procedure as above, the comparison is summarized below in Table 12. The difference is large but not unexpected.

Hypothetical Dust Devils	$\Delta P_{c/l}$ (Pa)	ρ_∞ (kg/m^3)	η_p (μs)	ν (m^2/s)	ν_{turb}/ν
Earth DD	250	1.471	24	1.048E-5	97
Mars DD	2.58	0.0167	36	7.33E-4	1.9

Table 12: Earth vs Mars dust devil comparison.

Comparing the percent difference in densities to the percent difference in viscosity ratios, which are 195% and 192% respectively, demonstrates the consistency of the Mars results with the terrestrial results obtained by Ash and Zardadkhan (2013). Interestingly, there is a matching correlation between vibrational absorptions. The vibrational absorption coefficient, α_{vib}, for Mars was estimated to be 10^{-2} Np/m versus 10^{-4} Np/m for Earth at an audible frequency of 500 Hz (Bass and Chambers, 2001). The percent difference here is 196% which suggests that the calculations are maintaining a consistent proportionality between Earth and Mars, further corroborating the reasonableness of the results.

5.2 Vortex Characteristics of Four Martian Dust Devils

Having established a level of confidence in the viscosity ratios and the estimates for η_p *and* η_v, the remaining relations from Ash, Zardadkhan, and Zuckerwar (2013), given in Section 2.1, have been employed; beginning with using ν_{turb} and η_p to find the maximum azimuthal or swirl velocity, $V_{\theta,max}$. In order to estimate circulation, Γ, circulation-based Reynolds number, R_Γ, angular velocity at the centerline, ω, and the maximum dust devil height, h_{max}, a core radius, r_{core}, is required. The diameters of the four Phoenix dust devils were estimated to be between 20 and 200 meters (Ellehoj, et al, 2010). Since correlated core radii specific to each event are not known, as a demonstration, Table 13 below shows the estimated physical characteristics for the r_{core} cases of 10 and 100 meters to cover the range estimated by Ellehoj, et al.

The maximum azimuthal velocity estimates are consistent with visual observations and tangential windspeed estimates of comparable events during the Pathfinder mission (Metzger et

al., 1999; Renno et al., 2000), as well as the general windspeed data collected during the Viking (Hess et al., 1977), Pathfinder (Schofield et al.,1997) and Phoenix (Holstein-Rathlou et al., 2010) missions. Reasonable results here indicate that this method can be applied to historical dust devil data, even without complete in-situ measurements and corresponding visual images. While these are estimates, processing old data would lead to a larger volume of information. Using this method to evaluate events where at least one physical dimension such as height or diameter is known, together with $T_\infty, P_\infty,$ and $\Delta P_{c/l}$, can be useful not only from a design perspective but also can potentially lead to a better understanding of how dust is transported in the Martian atmosphere.

	Dust Devil Event Sol			
Characteristic	**90**	**95**	**118**	**136**
$V_{\theta,max}$ (m/s)	8.80	10.43	8.36	8.66
r_{core} = 10 m				
Γ (m^2/s)	1106	1310	1051	1089
R_Γ	126,200	104,800	164,300	159,300
$\omega_{c/l}$ (rad/s)	1.76	2.085	1.673	1.732
h_{max} (m)	48	44	55	54
r_{core} = 100 m				
Γ (m^2/s)	11,060	13,100	10,500	10, 900
R_Γ	1,265,000	1,048,000	1,643,000	1,593,000
$\omega_{c/l}$ (rad/s)	0.1760	0.2085	0.1673	0.1732
h_{max} (m)	1,520	1,380	1,730	1,710

Table 13. Physical and vortex characteristics of four Phoenix Mission dust devils.

5.3 Martian Relative Humidity Influence

The influence of relative humidity on pressure relaxation at Mars was a major initial focus of this study. Despite the exceedingly small percentages of H_2O in the Martian atmosphere, the knowledge that RH strongly impacts pressure relaxation in the terrestrial atmosphere and the strong relaxation influence H_2O has on CO_2, initially motivated the effort to include RH considerations. The identification of three "humid zones" by B. Pal, et al. (2019) and shown in Figure 6 below, around Arabia Terra, Elysium Mons, and the region encircled by Amazonis, Alba Patera, and Tharsis, which remain supersaturated at night throughout the Martian year, further supports the suspicion that RH may be important.

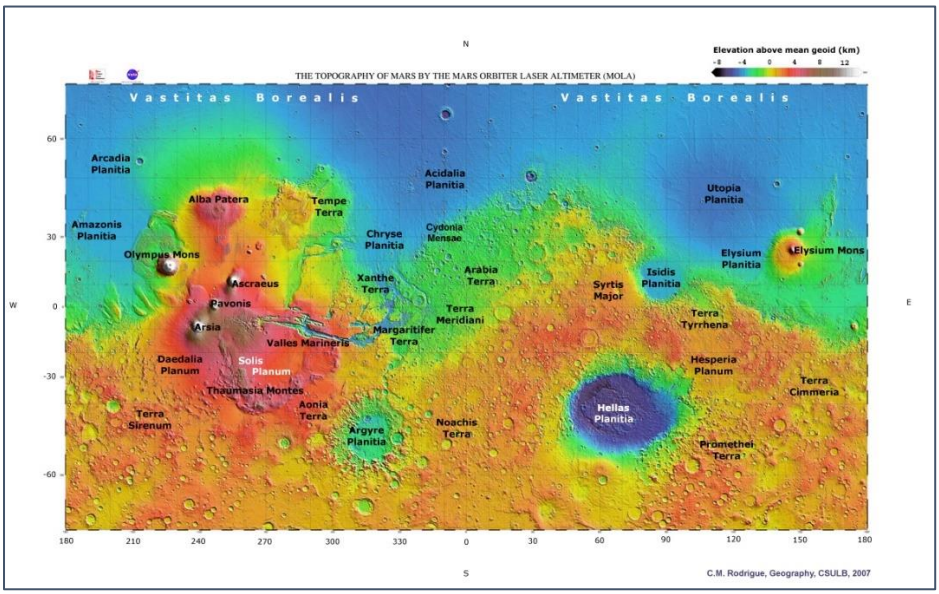

Figure 6: Global MOLA map with identifying regions (Rodrigue, 2007).

It has been expected and seemingly confirmed by orbiters and landers that Martian dust devils predominately occur in the daytime, peaking in midafternoon. However, the Phoenix

Lander recorded 29 smaller pressure events between the hours of 21:00 and 01:00. These events could have been a result of turbulent atmosphere passing over Heimdal Crater approximately 2 hours before passing over the lander (Ellehoj et al., 2010) and were largely disregarded. Furthermore, a recent study using a Martian Global Circulation Model (MGCM) to investigate the diurnal variations in dust devil activity showed multiple peaks of activity, not just during the expected afternoon hours when RH values are the lowest but also in the morning and late afternoon to evening hours (Chapman et al., 2017). The authors were able to corroborate most of their findings with historical Mars data, but due to the temporal limitations of orbital and in-situ missions they were unable unambiguously to show that the differences were not due simply to parameterization choices made with the MGCM (Chapman et al., 2017). Dust devil events during higher RH periods of the day cannot be ruled out; coupled with the extreme Martian diurnal variations, the continued consideration of relative humidity is justified. Understanding the impact RH may have on vortex structures in the Martian environment is not only important for this study, but also there is value in understanding its effects on relaxation processes in general as we continue exploration of the planet, particularly as we begin to explore aerially.

Zuckerwar and Ash (2009) predicted that the pressure relaxation term was dependent on the relative humidity of air, and their work indicated that as humidity increased the pressure relaxation coefficient decreased (See Table 14). The physical comparison on Earth being the difference in maximum heights between drier dust devils and their more humid counterparts, tornadoes.

	Relative humidity					
Temp	0%	20%	40%	60%	80%	100%
273.15 K	43.38	2.58	1.31	0.88	0.66	0.53
283.15 K	50.52	1.78	0.91	0.61	0.46	0.37
293.15 K	58.23	1.28	0.64	0.43	0.32	0.26
303.15 K	66.5	0.93	0.47	0.31	0.23	0.18
313.15 K	75.31	0.69	0.34	0.23	0.17	0.13
323.15 K	84.64	0.52	0.26	0.17	0.12	0.10

Table 14: Acoustically based estimates of the pressure relaxation coefficient for air at select temperatures and relative humidities (Ash, Zardadkhan, and Zuckerwar, 2011).

On Mars, the results are quite different. Figure 7 shows that RH has a negligible effect on the pressure relaxation coefficients, having less than 0.26% difference in η_p values over the logical temperature range of 215 K to 285 K at a reference pressure of 610 Pa.

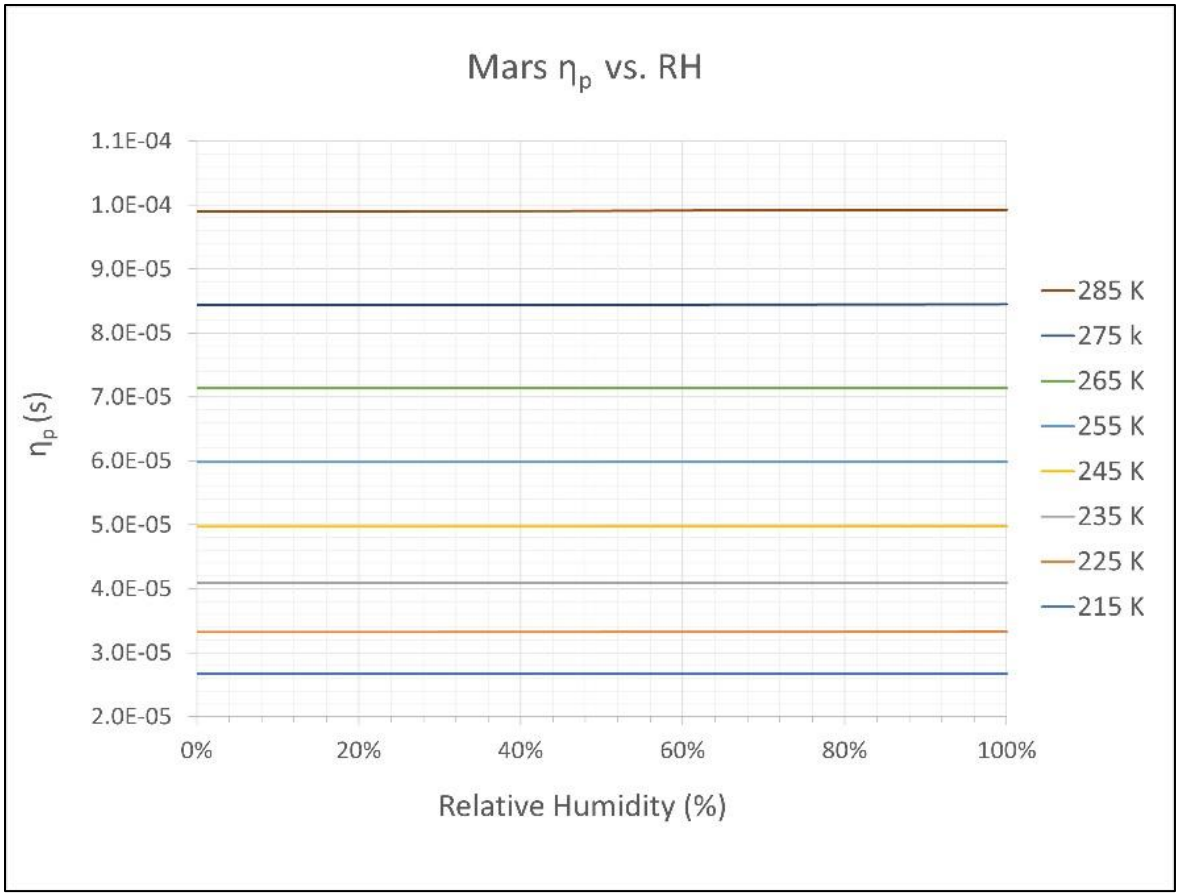

Figure 7: Pressure relaxation coefficient vs. relative humidity at 610 Pa and select temperatures.

As can be seen in Figure 8, the difference increases with increasing temperature. At most, even at the 310 K upper temperature limit on Mars, the difference does not exceed 1%.

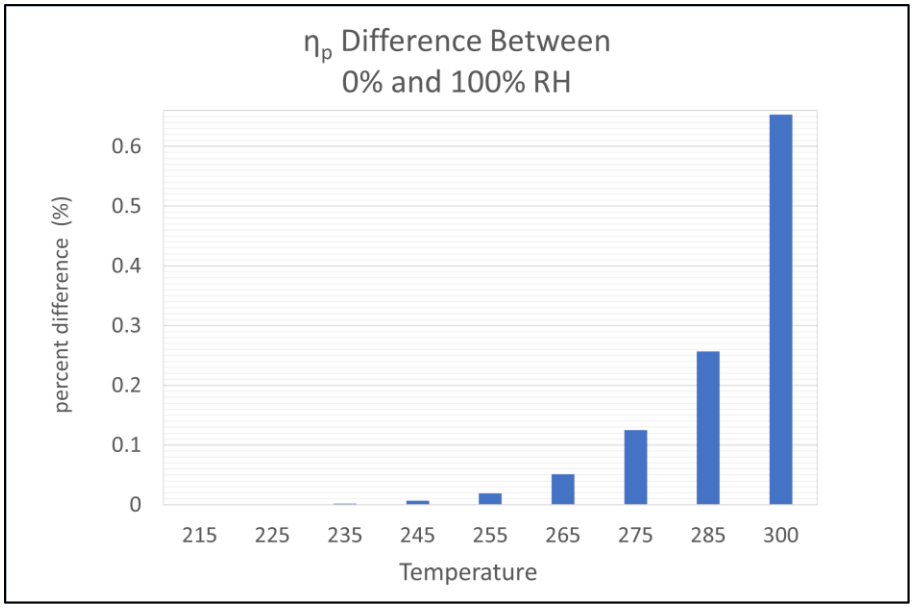

Figure 8: The effect of relative humidity on the pressure relaxation coefficient.

Repeating the calculations for the four Phoenix dust devils above without considering RH demonstrated a < 1% difference in h_{max}. Additionally, when disregarding RH and using the atmospheric model based on the global average H_2O contribution of 0.03% versus accounting for the seasonal and latitudinal variation in H_2O, the difference remained less than 1%. However, in this case there was significant variation, from 0.008 % to 0.24 % and while still small, a hypothetical dust devil case was added to discern the reason. The hypothetical dust devil

matches the conditions, based on season and location, of an observed event from HiRISE image PSP_004168_1220 (see section 7 below), chosen for its higher estimated ambient conditions.

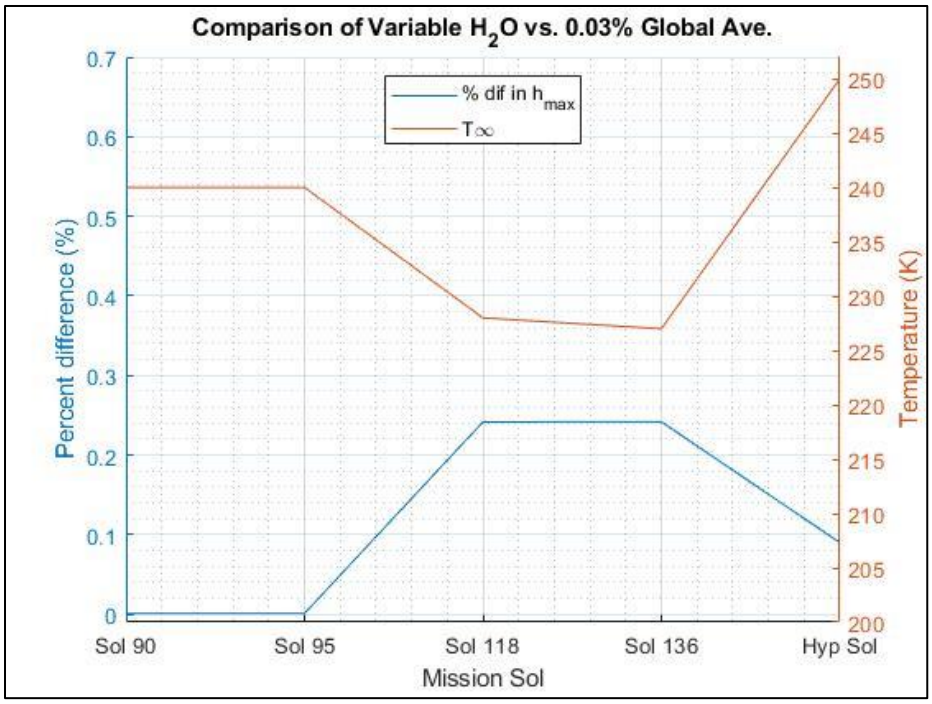

Figure 9: Comparison of results for hmax between Mars atmospheric composition models.

It is clear in Figure 9 that for the lower temperature events, the percent difference increases. Concerning the continuing study of the Martian atmosphere in general, this does imply that there may be situations when use of a variable H_2O model may be warranted, depending on the nature of the study. As it relates to this work the difference is small, meaning the thermophysical properties using the atmospheric composition model based on the globally averaged H_2O

contribution of 0.03% are adequate and RH data is not needed for the application of the Ash, Zardadkhan, and Zuckerwar model to Mars's atmosphere.

CHAPTER 6

APPLICATION EMPLOYING SATELLITE IMAGERY

In the previous sections the physical characteristics of Martian dust devils were estimated using the local temperature, local pressure, and the pressure change for an event. This section demonstrates the possibility for estimating the circulation, angular rotation rates, and pressure deficits based on height and footprint diameters obtained from satellite imagery or just employing the width of dust devil tracks, coupled with latitude and season.

Figure 10: Collection of HiRISE dust devil images (NASA/JPL/U of Arizona).

As examples, seven HiRISE images of active dust devils with known latitudes and areocentric longitudes (L_s) were selected. Their column heights and diameters were estimated in a 2011 study by measuring shadow lengths and accounting for illumination geometry (Choi and

Dundas, 2011). To proceed further, a local near surface temperature and pressure were needed and since accompanying thermal IR temperature estimates were not readily available, a seasonally appropriate estimate based on latitude and L_s was used from the daytime data compiled by M.D. Smith (2004). The temperature difference between night and day can vary significantly as seen in Figure 11, and as such this estimate is rough. The near surface pressures also vary greatly seasonally and latitudinally, but the diurnal variation is usually less than 10 Pa, justifying an average pressure at a given latitude and L_s plus 5 Pa for a daytime event. This average is taken from data compiled by F. Hourdin, et al. (1993).

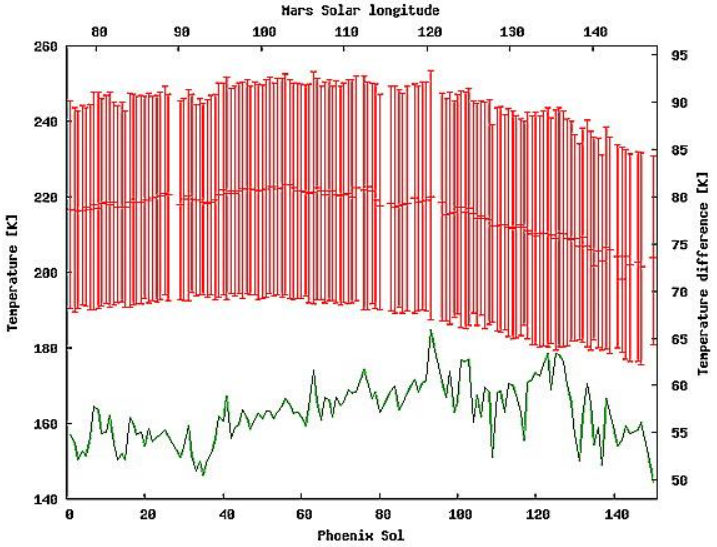

Figure 11: Diurnal temperature variations at the Phoenix Lander (Davy, et al., 2010).

The estimated temperatures and pressures were then used with the tables generated in Chapter 3 (Appendix A contains the complete table) to find η_p and the kinematic viscosity. Recalling the average viscosity ratio for Mars, ${}^{\nu_{turb}}/_{\nu} = 1.90 \pm 0.6$ from Section 6.1, relation (1.6)

can be employed to estimate the pressure drop, $\Delta P_{C/L}$ and subsequently, $V_{\theta,max}$ with (1.4), as Ash, Zardadkhan, and Zuckerwar provided a relationship between maximum swirl velocity, turbulent viscosity, and the pressure relaxation coefficient. Equation (1.4) also relates circulation, Γ_0, directly to the core radius and $V_{\theta,max}$. Similarly, from Eq. (1.9), the angular rotation rate about the centerline, ω, is twice the maximum swirl velocity divided by the core radius. The results are summarized in Table 15.

HiRISE image	**h** m	**r_{core}** m	**Lat.**	**L_s**	**~T_∞** K	**~P_∞** Pa	**$V_{\theta,max}$** m/s	**$\omega_{c/l}$** rad/s	**Γ_o** m^2/s	**$\Delta P_{C/L}$** Pa
PSP_004168_1220	150	15	57.9° S	259.1°	250	780	8.34	1.11	1570	2.27
PSP_009819_2130	650	125	32.8° N	120°	210	560	10.61	0.17	16,700	3.13
ESP_013199_1900	400	50	9.8° N	269.7°	225	665	9.60	0.38	6034	2.85
ESP_021925_1650	150	25	14.6° S	265.3°	230	625	9.32	0.75	2930	2.46
ESP_061787_2140	650	25	~33.8°N	~87°	200	680	11.39	0.91	3580	4.60
ESP_026051_2160	800	15	~30°N	~60°-70°	200	700	11.39	1.52	2150	4.74
Amazonis_Planitia (2012)	20k	70	~30°N	~83°	200	680	11.36	0.32	10,000	4.58

Table 15: Results for sample HiRISE Image cases.

The orbital images of dust devil tracks have intrigued researchers for decades, but with only an estimated diameter to mark the occurrence, their investigation has been limited. The tracks made by dust devils on Mars have been observed to change with time as surface winds, regional and global dust storms, and seasonal frost deposits erase them (Reiss et al., 2016).

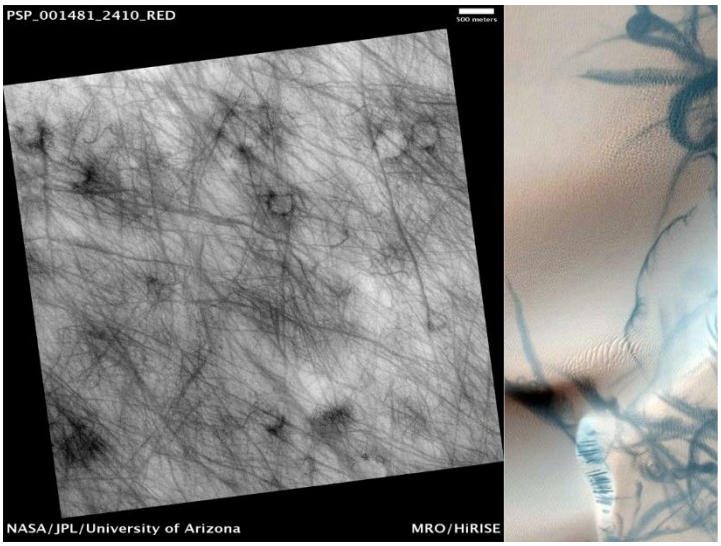

Figure 12: Examples of HiRISE imaged dust devil tracks (NASA/JPL/U of Arizona).

Based on this, many tracks can potentially be associated with a season. Table 16 shows the results for three hypothetical historical events leaving tracks of different widths by following the same procedure just described but with the additional step of employing the Mars relation for h_{max}, Eq. (5.1), to estimate the height of the hypothetical dust devil. For simplicity, the events are similar in season and latitude to some of the dust devils in the images from Table 15. Dust devil tracks can range in width from ~1 m to 1 km (Reiss et al., 2016).

Dust Devil Track	**Width** m	**Lat.**	**L_s**	**~T_∞** K	**~P_∞** Pa	**$V_{\theta,max}$** m/s	**$\omega_{c/l}$** rad/s	**Γ_o** m^2/s	**$\Delta P_{C/L}$** Pa	**h_{max}** m
Track 1	200	57.9° S	259.1°	245	750	8.56	0.17	10,800	2.34	1,455
Track 2	500	9.8° N	269.7°	228	680	9.44	0.08	29,650	2.77	6,180
Track 3	1000	32.8° N	120°	210	560	10.59	0.04	66,600	3.12	18,250

Table 16: Estimated vortex characteristics for 3 hypothetical dust devil tracks.

The track widths chosen for the hypothetical cases range from 200 m to 1000 m, representing some of the largest orbital image observations. The estimated maximum heights in Table 16 are consistent with the range of heights observed over the years, from hundreds of meters to tens of km (Bell, T., 2005); a notable example of the high end of this range being the nearly 20,000 m dust devil spotted by HiRISE in 2012 (Geissler, 2012). Using this method could be a simple way to quickly add to the current volume of knowledge on these giant devils.

CHAPTER 7

CONCLUSIONS AND DISCUSSION

A systematic and meticulous approach was taken when applying the non-equilibrium model developed by Ash, Zuckerwar, and Zardadkhan to the case of Mars's dust devils. Their work showed that fundamental flow processes can be controlled by non-equilibrium pressure forces, offering a consistent physical description for the non-physical flow of the Rankine Vortex model. The exact solution of the modified Navier-Stokes equations for axial filaments (Ash, Zardadkan, and Zuckerwar, 2011) and later for an axisymmetric rotating flow above a fixed ground plane (Ash and Zardadkan, 2013), provided useful and simple relations for the estimation, analysis, and characterization of key physical attributes of terrestrial dust devils. The results of this work demonstrate the Ash, Zardadkhan, and Zuckerwar method can be successfully applied to Mars. With the highlighted practical applications in sections 6.2 and 7 as examples of how it can be employed, it is hoped that this method can contribute greatly to our ever-growing wealth of knowledge of Mars and to the challenges we face as mankind continues to explore.

Some key differences between the Martian and terrestrial cases were found in the course of this study, particularly regarding the effect of relative humidity on pressure relaxation. On Earth, for moist air, η_p decreases as temperature increases, and for dry air η_p increases as temperature increases. This, for terrestrial flows, explains in part why the stagnation plane, or h_{max}, at the top of a ground-coupled rotating flow is much smaller for dust devils than tornadoes. It was determined in this work that relative humidity has a negligible effect on the pressure relaxation parameter in the Martian environment and thus by extension, the absorption of sound. Figure 6 showed that as temperature increased, η_p increased, corresponding to the results in Tables 15 and 16, where the dust devils with higher maximum heights also were associated with the lowest ambient temperatures (T_∞).

Examining again relations (3.19) through (3.26), note there is both a temperature and pressure dependency in the pressure relaxation coefficient. Keeping temperature constant and varying pressure shows that an increase in pressure produces a reduction in η_p. While temperature is the dominant parameter, pressure could be more of a factor on Mars than on Earth due to the magnitude of seasonal variations of Martian atmospheric pressure and associated global pressure ranges. The seasonal variation is much smaller on Earth, < 3% (Rafferty,

J.,2020), versus ~32% on Mars (Hourdin, et al., 1993), as is the range for minimum and maximum surface pressures; a low of 870 hPa and high of 1081.2 hPa for Earth versus a low and high of 0.7 hPa and 14 hPa respectively for Mars. Thus, the results in this work suggest not only that dust devils developing under lower temperature conditions are larger and stronger, but when the local pressure is also near or higher than 1 Mars atm (610 Pa), there is an increased potential for giant devils to form. Consider Track 3 from Table 15, using a higher pressure of ~740 Pa. This would result in a nearly 3000 m predicted increase in h_{max}.

The colder temperatures and larger pressure variations provide some explanation for the differences in maximum heights between Mars's dust devils and their terrestrial cousins, but there must be more. There is a clear proportional relationship between the stagnation height and core radius through the angular rotation rate, eqns. (2.8) and (2.9); however, comparing the Amazonis Planitia dust devil from Table 14 and Track 3 from Table 15, with their similar heights and drastically different core radii, draws attention to their formation. On Earth, dust devils need calm winds to form (Sinclair, 1969), and their rotation begins as the rising warmer air begins to stretch, cool, and then fall, generating vorticity. This sensitivity is thought to be due to enhanced mechanical mixing, and the disruption of the organized dynamical structures (Rafkin, et al., 2016).

Windspeeds on Mars are rarely calm during daytime hours, when dust devil activity is most common, with average windspeeds often above 4 m/s, ranging as high as 16 m/s throughout the Phoenix mission (Holstein-Rathlou, C., et al., 2010). Additionally, a correlation was found between increased dust devil activity and an increase in ambient wind speeds (Ellehoj, et al., 2010). The MGCM simulation study corroborated this aspect of Ellehoj's observations which may suggest that on Mars windspeeds may be more of a driving force than variable surface heating (Chapman et al., 2017). If true, this implies that wind shear helps to organize the vortical structure rather than disrupt it as on Earth.

Convective vortical flows that occur on both Earth and Mars appear similar but have clear differences in atmospheric behavior, global weather impact, and possibly formation processes. This thesis provides a tool that can be employed to evaluate past, present, and future data acquired both in situ and remotely. Adding to the volume of information already accumulated over the decades of Mars's exploration is crucial to advancing our understanding of its environmental processes. More knowledge often leads to more questions, and it is hoped that

this tool will lead to both, as this is the best way to fully understand the challenges we face as mankind continues to explore.

7.1 Future Work

The current work, as it pertains to exploration of Mars can be extended to explore more of the unanswered questions about these flows in the Martian environment in at least a few ways. The entrainment of dust from the regolith, on Earth and Mars, by these vortical flows is the reason they are visible and thusly named. The rubbing together of the dust and sand particles can produce a triboelectric charging effect and based on the documented presence of electrostatic and electromagnetic fields in terrestrial dust devils (Farrell, et al., 2004), and the high electric conductivity of Mars atmosphere, the Ash and Zardadkhan model (2013) could be modified to incorporate magnetic and electric field components. This would explore the possibility of Mars's dust devils behaving as magnetic solenoids and whether a generated magnetic field and triboelectric charging contributes to the extreme heights of Martian dust devils and dust lifting.

Scientists generally believe dust devils contribute to weather patterns on Mars through dust transport, but can giant dust devils trigger the larger planet-wide dust storms? The enormous scale of this phenomena alone, warrants investigation, and understanding its genesis would be helpful. For perspective, Figure 13 shows two images of the same region, before and after a global dust storm.

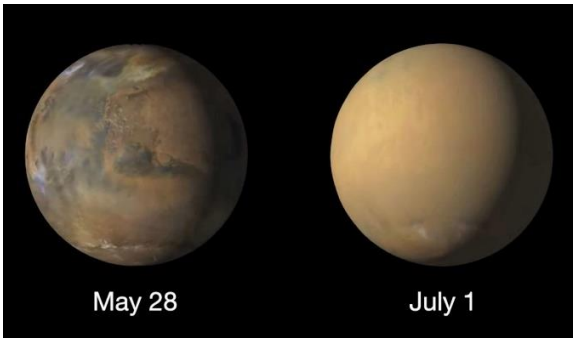

Figure 13: Before and after images of a Mars global dust storm (NASA/JPL/ Mars color Imager MRO).

The maximum swirl velocities in most Martian dust devils do not reach the threshold for dust lifting, which is estimated to be ~30 m/s (Greeley , et al., 2003) for the 1-4 μm sized particles. Suction by the low-pressure core has been suggested by Greeley et al. (2003, 2006) as the explanation for the lifting that clearly occurs, but considering the heights of the giant devils, it stands to reason that there may be other factors. Learning more about Martian dust devils and their impact on Mars's weather patterns could be invaluable in the design of future missions as well as atmospheric simulation modeling.

REFERENCES

ANSI-ASA S1.26 – 2014 (2014). "Method for calculation of the absorption of sound by the atmosphere," *Standards Secretariat of the Acoustical Society of America*, New York.

ASH, R.L., ZARDADKHAN, I., and ZUCKERWAR, A.J. (2011). "The influence of pressure relaxation on the the structure of an axial vortex," *Physics of Fluids* 23, 073101.

ASH, R.L., ZARDADKHAN, I. (2013). "Non-equilibrium pressure control of the height of a large-scale, gound-coupled, rotating fluid column," *Physics of Fluids* 25, 053101.

ASH, R.L., ZARDADKHAN, I. (2021). "Non-equilibrium behavior of large-scale axial vortex cores," *AIP Advances* 11, 025320.

ATKINS, P., de PAULA, J., and KEELER, J. 2018. *Atkins' Physical Chemistry Volume 2: Quantum Chemistry, Spectroscopy, and Statistical Thermodynamics*, 11th Edition, pg. 602.

BAKER, C.J., STERLING, M. (2017). "Modeling wind fields and debris flight in tornadoes," *J. Wind Eng. Ind. Aerod.* 168, pp. 312-321.

BALME, M., and GREELEY, R. (2006). "Dust devils on Earth and Mars," *Reviews of Geophysics*, 44, RG3003.

BARLOW, N. (2008). Mars: An introduction to its interior, surface and atmosphere, Cambridge University Press, pg. 164.

BASS, H.E., CHAMBERS, J.P. (2001). "Absorption of sound in the Martian atmosphere," *The Journal of the Acoustical Society of America* 109, 3069.

BAUER, H.J. (1965). (in) Physical Acoustics, W.P. Mason, Ed. (Academic, New York, 1965), Vol. 2, Part A, Chapter 2, Sec. E.

BELL, T. (2005). "The Devils of Mars", Published July, 14, 2005, *@Science.NASA*.

BÜCKER, SPAN, R., and WAGNER, W. (2003). "Thermodynamic property models for moist air and combustion gases," *ASME Journal of Engineering for Gas Turbines and Power*, Vol. 125.

BURGERS, J.M. (1948). "A mathematical model illustrating the theory of turbulence," *Advanced Applied Mechanics* 1, pp. 171-199.

CARR, M.H. (2006). The Surface of Mars, Cambridge University Press, New York.

CATLING, D.C. (2014). (in) T. Spohn, D. Breur & T.V. Johnson (Eds), Encyclopedia of the Solar System , Elsevier, Chapter 16, pp. 343-357.

CHAPMAN, R.M., LEWIS, S.R., BALME, M. and STEELE, L.J. (2017). "Diurnal variation in Marian dust devil activity," Icarus, 292, pp. 154-167.

CHOI, D.S., DUNDAS, C.M. (2011). "Measurements of Martian dust devil winds with HiRISE," *Geophysical Research Letters* 38, L24206.

CRC (Chemical Rubber Company) (1984). CRC Handbook of Chemistry and Physics. Weast, Robert C., editor. 65th edition. CRC Press, Inc. Boca Raton, Florida. USA.

CRIFO, J.F. (1989) "Inferences concerning water vapor viscosity and mean free path at low temperatures," *Astronomy and Astrophysics* 223, pp. 365-368.

CURRAN, R.J., CONRATH, B.J., HANEL, R.A., KUNDE, V.G., PEARL, J.C. (1973). "Mars: Mariner 9 spectroscopic evidence for H_2O ice clouds," *Science*, Vol. 182, Issue 4110.

DAVIDSON, T.A. (1993). "A Simple and Accurate Method for Calculating Viscosity of Gaseous Mixtures", United States Department of the Interior; Bureau of Mines.

DAVY, R., DAVIS, J., TAYLOR, P., LANGE, C., WENG, W., WHITEWAY, J., GUNNLAUGSON, H. (2010). "Initial analysis of air temperature and related data from the Phoenix MET station and their use in estimating turbulent heat fluxes," *Journal of Geophysical Research*, Vol. 115, E00E13.

ELLEHOJ, M.D., GUNNLAUGSSON, H.P., TAYLOR, P.A., KAHANPÄÄ, H., BEAN, K.M., CANTOR, B.A., GHEYNANI, B.T., DRUBE, L., FISHER, D., HARRI, A.M., HOLSTEIN-RATHLOU, C., LEMMON, M.T., MADSEN, M.B., MALIN, M.C., POLKKO, J., SMITH, P.H., TAMPPARI, L.K., WENG, W., WITEWAY, J., (2010). "Convective vortices and dust devils at the Phoenix Mars mission landing site," *Journal of Geophysical Research*, Vol. 115, E00E16.

FARRELL, W.M., SMITH, P.H., DELORY, G.T., HILLARD, G.B., MARSHALL, J.R, CATLING, D., HECT, M., TRATT, D.M., RENNÓ, N., DESCH, M.D., CUMMER, S.A., HOUSER, J.G, JOHNSON, B. (2004). "Electric and magnetic signatures of dust devils from the 2000-2001 MATADOR desert tests," *Journal of Geophysical Research*, Vol. 109, E03004.

FISCHER, E., MARTÍNEZ, G.M., RENNÓ, N.O., TAMPPARI, L.K., ZENT, A.P. (2019). "Relative humidity on Mars: New results from the Phoenix TECP sensor," *Journal of Geophysical Research: Planets*, Vol. 124, pp. 2780-2792.

GEISSLER, P. (2012). "A Monster Dust Devil Stalks the Martian Landscape," University of Arizona/ LPL/JPL/HiRISE.

GILLMEIER, S., STERLING, M., HEMIDA, H., BAKER, C.J. (2018). "A reflection on analytical tornado-like vortex flow field models," *Journal of Wind Engineering and Industrial Aerodynamics*, Volume 174, pp. 10-27.

GOFF, J.A. (1965). "Saturation pressure of water on the new Kelvin scale," in *Humidity and Moisture: Measurement and control in science and industry*, Vol. 3, Ed. A. Wexler, Reinhold Publishing, New York.

GOFF, J.A., GRATCH, S. (1946). "Low-pressure properties of water from -160 to 212 F," *Trans. Am. Soc. Heating Air-Cond. Eng.*, Vol. 52, pp. 95-122.

GORTLER, H., (1954). "Decay of swirl in axially symmetrical jet, far from the orifice," *Revista Matematica Hispano-Americana*, Vol. 14, pp. 143-178.

GREELEY, R., BALME, M.R., IVERSON, J.D., METZGER, S., MICKELSON, R., PHOREMAN, J., WHITE, B., (2003). " Martian dust devils: Laboratory simulations of particle threshold," *Journal of Geophysical Research*, Vol. 108, E55041.

GREELEY, R., WHELLEY, P., ARVIDSON, R., CABROL, N., FOLEY, D., FRANKLIN, B., GEISSLER, P., GOLOMBEK, M., KUZMIN, R., LANDIS, G., LEMMON, M., NEAKRASE, L., SQUIRES, S., THOMPSON, S. (2006). "Active dust devils in Gusev crater, Mars: Observations from the Mars exploration rover Spirit," Journal of Geophysical Research, Vol. 111, E12S09.

HABERLE, R., CLANCY, R., FORGET, F., SMITH, M., and ZUREK, R. eds. (2017). The Atmosphere and Climate of Mars, Cambridge University Press, Cambridge.

HARRIS, C.M. (1967). "Absorption of sound in air versus humidity and temperature," Columbia University for George C. Marshall Space Flight Center, NASA CR-647.

HERNING, F., ZIPPERER, L. (1936). "Calculation of the viscosity of technical gas mixtures from the viscosity of the individual gases," *Gas-und Wasserfach*, Vol. 79, pp. 69-73.

HERZFELD, K.F., RICE, F.O. (1928). "Dispersion and absorption of high frequency sound waves," *Physical Review*, 31, pg. 691.

HESS, S.L., HENRY, R.M., LEOVY, C.B., RYAN, J.A., TILLMAN, J.E. (1977). "Meteorological results from surface of Mars: Viking 1 and 2," *Journal of Geophysical Research*, Vol. 82, pp. 4559-4574.

HOLSTEIN-RATHLOU, C., GUNNLAUGSSON, H.P., MERRISON, J.P., BEAN, K.M., CANTOR, B.A., DAVIS, J.A., DAVY, R., DRAKE, N.B., ELLEHOJ, M.D., GOETZ, W., HVIID, S.F., LANGE, C.F., LARSEN, S.E., LEMMON, M.T., MADSEN, M.B., MALIN, M., MOORES, J.E., NORNBERG, P., SMITH, P., TAMPPARI, L.K., TAYLOR, P.A. (2010). "Winds at the the Phoenix landing site," *Journal of Geophysical Research*, Vol. 115, E00E18.

HOURDIN, F., LeVAN, P., FORGET, F., TALAGRAND, O. (1993). "Meteorological variability and the annual surface pressure cycle on Mars," *Journal of Atmospheric Science*, 50, pp. 3625-3640.

JACKSON, B., LORENZ, R., DAVIS, K. (2018). "A Framework for relating the structures and recovery statistics in pressure-time series for dust devils," *Icarus*, 299, pp. 166-174.

JACOB, D. (1999). Introduction to Atmospheric Chemistry, Princeton University Press.

JAEGER, F., MATAR, O., MÜLLER, E. (2018). "Bulk viscosity of molecular fluids," *J. Chem. Phys*., 148, 174504.

KNUDSEN, V.O. (1931). "The effect of humidity upon the absorption of sound in a room," *Journal of the Acoustical Society of America*, Vol. 3, pg. 126.

LAMB, H. (1932). Hydrodynamics, 6th Edition, Cambridge University Press.

LAMB, J. (1965). in *Physical Acoustics*, Vol. 2-A, Edited by W.P. Mason (Academic, New York).

LANDAU, L., TELLER, E. (1936) . Phys. Z. Sow., 10, pg. 34.

LENTE, G., ŐSZ, K. (2020). "Barometric formulas: various derivations and comparisons to environmentally relevant observations," ChemTexts (2020) 6:13.

LEWIS, J., LEE, K.P. (1965). "Vibrational relaxation in carbon dioxide/water-vapor mixtures," *Journal of the Acoustical Society of America*, Vol. 38, pg. 813.

MARTÍNEZ, G.M., NEWMAN, C.N., DE VICENTE-RETORILLO, A., FISCHER, E., RENNO, N.O., RICHARDSON, M.I., FAIRÉN, A.G., GENZER, M., GUZEWICH, S.D., HABERLE, R.M., HARRI, A.-M., KEMPPINEN, O., LEMMON, M.T., SMITH, M.D., de la TORRE-JUÁREZ, M., VASAVADA, A.R. (2017). "The modern near-surface Martian climate: A review of in-situ meteorological data from Viking to Curiosity," *Space Science Review*, 212, pp. 295-338.

METZGER, S.M., CARR, J.R., JOHNSON, J.R., PARKER, T.J., LEMMON, M.T. (1999). "Dust devil vortices seen by the Mars Pathfinder camera," *Geophysical Research Letters*, 26(18), pp. 2781-2784.

MURPHY, D.M., KOOP, T. (2005). "Review of the vapour pressures of ice and supercooled water for atmospheric applications," *Q. J. R. Meteorological Society*, 131, pp. 1539-1565.

PÁL, B., KERESZTURI, Á., FORGET, F., SMITH, M.D. (2019). "Global seasonal variations of the near-surface relative humidity levels on present day Mars," Icarus 333, pp. 481-495.

RAFFERTY, J. (2020). Ed. "Atmospheric Pressure," Encyclopedia Britannica. (Accessed, 3 April 2021).

RAFKIN, S., JEMMETT-SMITH, B., FENTON, L. (2016). "Dust devil formation," *Space Science Review*, 203, pp. 183-207.

REISS, D., HOEKZEMA, N.M., STENZEL, O.J. (2014). "Dust deflation by dust devils on Mars derived from optical depth measurements using the shadow method in HiRISE images," *Planetary and Space Science*, 93-94, pp. 54-64.

RENNO, N.O., NASH, A.A, LUNINE, J., MURPHY, J. (2000). "Martian and terrestrial dust devils: Test of a scaling theory for dust devils," *Journal of Geophysical Research*, Vol. 105, pp. 1859-1865.

RIVERA-VALENTÍN, E.G., GOUGH, R.V., CHEVRIER, V.F., PRIMM, K.M., MARTINEZ, G.M., TOLBERT, M. (2018) . "Constraining the potential liquid water environment at Gale crater, Mars," *Journal of Geophysical Research: Planets*, 123, pp. 1156–1167.

ROGERS, G.F.C., MAYHEW, Y.R. Eds. (1995). "Thermodynamic and Transport Properties of Fluids," Fifth Edition, Blackwell Publishing Ltd.

ROTT, N. (1958). "On the viscous core of a line vortex," *Zeitschrift fur Angewandte Mathematik und Physik*, Vol. 9b, pp. 543-553.

SCHOFIELD. J.T., BARNES, J.R., CRISP, D., HABERLE, R.M., LARSEN, S., MAGALHAES, J.A., MURPHY, J.R., SEIFF, A., WILSON, G. (1997). "The Mars Pathfinder atmospheric structure investigation meteorology (ASI/MET) experiment," *Science*, 278(5344), pp. 1752-1758.

SCHWARTZ, R., SLAWSKY, Z., HERZFELD, K. (1952). "Calculation of vibrational relaxation times in gases," *J. Chem. Phys.* 20, pp. 1591–1599.

SHEILDS, F.D., WARF, C.C., BASS, H.E. (1973). "Acoustical method of obtaining vibrational transition rates tested on CO_2/N_2 mixtures," *J. Chem. Physics*, Vol. 58, pp. 3837-3840.

SINCLAIR, P.C. (1969). "General characteristics of dust devils," *Journal of Applied Meteorology*, 8(1), pp. 32-45.

SINCLAIR, P.C. (1973). "Lower structure of dust devils," *Journal of Atmospheric Science*, 30(8), pp. 1599-1619.

SMITH, M.D. (2002). "The annual cycle of water vapor on Mars as observed by the Thermal Emission Spectrometer," *Journal of Geophysical Research: Planets*, Vol. 107, pg. 5115.

SMITH, M.D. (2004). "Interannual variability in TES atmospheric observations of Mars during 1999-2003," Icarus 167, pp. 148-165.

STULL, R. (2015). in Meteorology for Scientists and Engineers, 3rd Edition, Ch. 4, pp. 91-92.

SUTHERLAND, W. (1893). "The viscosity of gases and molecular force", Philosophical Magazine, S. 5, 36, pp. 507-531.

SULLIVAN, R.D. 1959. "A two cell vortex solution of the Navier-Stokes equations," *J. Areo. Sci.* 26, pp. 767-768.

THOMAS, P.C., GIERASCH, P.J. (1985). "Dust devils on Mars," *Science*, Vol. 230, pp. 175-177.

TISZA, L. (1942). "Supersonic absorption and Stokes' viscosity relation," *Physical Review*, Vol. 61, 531.

TRAINER, M., WONG, M., McCONNOCHIE, T., FRANZ, H., ATREYA, S., CONRAD, P., LEFEVRE, F., MAHAFFY, P., MALESPIN, C., MANNING, H., MARTIN-TORRES, J., MARTINEZ, G., McKAY, C., NAVARRO-GONZALEZ, R., VICENTE-RETORTILLO, A., WEBSTER, C., ZORZANO, M. (2019). "Seasonal variations in atmospheric composition as measured in Gale Crater, Mars," *Journal of Geophysical Research: Planets*, Vol. 124, Issue 11, pp. 3000-3024.

TROKHIMOVSKIY, A., FEDOROVA, A., KORABLEV, O., MONTMESSIN, F., BERTAUX, J., RODIN, A., SMITH, M.D. (2015). "Mars' water vapor mapping by the SPICAM IR spectrometer: Five Martian years of observations," Icarus, 251, pp. 50-64.

ZENT, A.P., HECHT, M.H., COBOS, D.R, WOOD, S.E., HUDSON, S.M., MILKOVICH, S.M., DeFLORES, L.P., MELLON, M.T. (2010). "Initial results from the thermal and electrical conductivity probe (TCEP) on Phoenix*," Journal of Geophysical Research*, Vol, 115, E00E14.

ZENT, A.P., HECHT, M.H., HUDSON, T.L., WOOD, S.E., CHEVRIER, V.F. (2016). "A revised calibration function and results for the Phoenix mission TCEP relative humidity sensor," *Journal of Geophysical Research: Planets*, Vol. 121, pp. 626-651.

ZUCKERWAR, A.J., ASH, R.L., (2006). "Variational approach to the volume viscosity of fluid," *Physics of Fluids* 18, 047101.

ZUCKERWAR, A.J., ASH, R.L., (2009). "Volume viscosity of fluids with multiple dissipative processes," *Physics of Fluids* 21, 033105.

ZUCKERWAR, A.J., MERIDETH, R.W., (1984). "Low-frequency sound absorption measurements in air," NASA Reference Publication RP-1128.

APPENDICES

A. Select Thermophysical Properties for Mars

Temp K	p_{sat}/p_r[a] (over ice)	c_p CO_2	c_v CO_2	c_p^0 Mars atm.	c_v^0 Mars atm.	c speed of sound	c_{vib}	**μ** Mars atm.	$P_\infty * \tau_{VT}$
180	0.00003	713.61	524.69	716.93	525.69	216.82	52.39	9.06E-06	0.00717
181	0.00004	714.60	525.68	717.88	526.64	217.37	53.38	9.11E-06	0.00739
182	0.00005	715.59	526.67	718.84	527.60	217.92	54.37	9.17E-06	0.00762
183	0.00006	716.59	527.67	719.81	528.57	218.46	55.37	9.22E-06	0.00785
184	0.00007	717.59	528.67	720.77	529.53	219.01	56.37	9.28E-06	0.00808
185	0.00008	718.60	529.68	721.74	530.50	219.55	57.38	9.33E-06	0.00832
186	0.00010	719.60	530.68	722.72	531.48	220.09	58.38	9.38E-06	0.00857
187	0.00012	720.62	531.70	723.70	532.46	220.62	59.40	9.44E-06	0.00882
188	0.00014	721.63	532.71	724.68	533.44	221.16	60.41	9.49E-06	0.00907
189	0.00016	722.65	533.73	725.67	534.43	221.69	61.43	9.54E-06	0.00934
190	0.00020	723.68	534.76	726.65	535.41	222.22	62.46	9.60E-06	0.00960
191	0.00023	724.70	535.78	727.65	536.41	222.75	63.48	9.65E-06	0.00988
192	0.00027	725.73	536.81	728.64	537.40	223.28	64.51	9.70E-06	0.01016
193	0.00032	726.77	537.85	729.64	538.40	223.81	65.55	9.76E-06	0.01044
194	0.00038	727.80	538.88	730.64	539.40	224.33	66.58	9.81E-06	0.01073
195	0.00045	728.84	539.92	731.64	540.40	224.86	67.62	9.86E-06	0.01103
196	0.00052	729.88	540.96	732.65	541.41	225.38	68.66	9.92E-06	0.01133
197	0.00061	730.92	542.00	733.65	542.41	225.90	69.70	9.97E-06	0.01164
198	0.00072	731.96	543.04	734.66	543.42	226.41	70.74	1.00E-05	0.01196
199	0.00084	733.01	544.09	735.67	544.43	226.93	71.79	1.01E-05	0.01228
200	0.00098	734.06	545.14	736.68	545.44	227.45	72.84	1.01E-05	0.01261
201	0.00114	735.11	546.19	737.70	546.46	227.96	73.89	1.02E-05	0.01294
202	0.00133	736.16	547.24	738.71	547.47	228.47	74.94	1.02E-05	0.01328
203	0.00154	737.21	548.29	739.73	548.49	228.98	75.99	1.03E-05	0.01363
204	0.00179	738.26	549.34	740.75	549.51	229.49	77.04	1.03E-05	0.01399
205	0.00207	739.32	550.40	741.77	550.53	229.99	78.10	1.04E-05	0.01435
206	0.00240	740.38	551.46	742.79	551.55	230.50	79.16	1.04E-05	0.01472
207	0.00277	741.43	552.51	743.81	552.57	231.00	80.21	1.05E-05	0.01510
208	0.00320	742.49	553.57	744.83	553.59	231.51	81.27	1.05E-05	0.01548
209	0.00368	743.55	554.63	745.85	554.61	232.01	82.33	1.06E-05	0.01587
210	0.00423	744.61	555.69	746.88	555.64	232.51	83.39	1.07E-05	0.01627
211	0.00486	745.67	556.75	747.90	556.66	233.00	84.45	1.07E-05	0.01667
212	0.00558	746.73	557.81	748.92	557.69	233.50	85.51	1.08E-05	0.01709

a. p_r -reference pressure for Mars is 610 Pa.

Select Thermophysical Properties for Mars (continued)

Temp K	p_{sat}/p_r[a] (over ice)	c_p CO_2	c_v CO_2	c_p^0 Mars atm.	c_v^0 Mars atm.	c speed of sound	c_{vib}	**μ** Mars atm.	$P_\infty * \tau_{VT}$
213	0.00639	747.78	558.86	749.95	558.71	234.00	86.56	1.08E-05	0.01751
214	0.00732	748.84	559.92	750.97	559.73	234.49	87.62	1.09E-05	0.01794
215	0.00836	749.90	560.98	752.00	560.76	234.98	88.68	1.09E-05	0.01837
216	0.00955	750.96	562.04	753.02	561.78	235.47	89.74	1.10E-05	0.01882
217	0.01088	752.02	563.10	754.04	562.80	235.96	90.80	1.10E-05	0.01927
218	0.01239	753.08	564.16	755.07	563.83	236.45	91.86	1.11E-05	0.01973
219	0.01410	754.14	565.22	756.09	564.85	236.94	92.92	1.11E-05	0.02020
220	0.01602	755.20	566.28	757.11	565.87	237.43	93.98	1.12E-05	0.02067
221	0.01818	756.26	567.34	758.13	566.89	237.91	95.04	1.12E-05	0.02116
222	0.02060	757.31	568.39	759.16	567.92	238.39	96.09	1.13E-05	0.02165
223	0.02333	758.37	569.45	760.18	568.94	238.88	97.15	1.13E-05	0.02215
224	0.02638	759.42	570.50	761.20	569.96	239.36	98.20	1.14E-05	0.02267
225	0.02981	760.48	571.56	762.21	570.97	239.84	99.26	1.14E-05	0.02318
226	0.03364	761.53	572.61	763.23	571.99	240.32	100.31	1.15E-05	0.02371
227	0.03792	762.58	573.66	764.25	573.01	240.79	101.36	1.15E-05	0.02425
228	0.04271	763.63	574.71	765.26	574.02	241.27	102.41	1.16E-05	0.02480
229	0.04805	764.68	575.76	766.28	575.04	241.75	103.46	1.16E-05	0.02535
230	0.05400	765.73	576.81	767.29	576.05	242.22	104.51	1.17E-05	0.02592
231	0.06063	766.78	577.86	768.30	577.06	242.69	105.56	1.17E-05	0.02649
232	0.06800	767.82	578.90	769.31	578.07	243.17	106.60	1.18E-05	0.02707
233	0.07620	768.87	579.95	770.32	579.08	243.64	107.65	1.18E-05	0.02766
234	0.08530	769.91	580.99	771.32	580.08	244.11	108.69	1.19E-05	0.02827
235	0.09540	770.95	582.03	772.33	581.09	244.57	109.73	1.19E-05	0.02888
236	0.10659	771.98	583.06	773.33	582.09	245.04	110.76	1.20E-05	0.02950
237	0.11898	773.02	584.10	774.33	583.09	245.51	111.80	1.20E-05	0.03013
238	0.13269	774.05	585.13	775.33	584.09	245.97	112.83	1.21E-05	0.03077
239	0.14785	775.09	586.17	776.33	585.09	246.44	113.87	1.22E-05	0.03143
240	0.16458	776.12	587.20	777.32	586.08	246.90	114.90	1.22E-05	0.03209
241	0.18305	777.14	588.22	778.32	587.08	247.36	115.92	1.23E-05	0.03276
242	0.20342	778.17	589.25	779.31	588.07	247.83	116.95	1.23E-05	0.03344
243	0.22585	779.19	590.27	780.30	589.06	248.29	117.97	1.24E-05	0.03413
244	0.25054	780.21	591.29	781.28	590.04	248.74	118.99	1.24E-05	0.03484
245	0.27770	781.23	592.31	782.27	591.03	249.20	120.01	1.25E-05	0.03555

a. p_r -reference pressure for Mars is 610 Pa.

Select Thermophysical Properties for Mars (continued)

Temp K	p_{sat}/p_r[a] (over ice)	c_p CO_2	c_v CO_2	c_p^0 Mars atm.	c_v^0 Mars atm.	c speed of sound	c_{vib}	μ Mars atm.	$P_\infty * \tau_{VT}$
246	0.30754	782.25	593.33	783.25	592.01	249.66	121.03	1.25E-05	0.03628
247	0.34031	783.26	594.34	784.23	592.99	250.12	122.04	1.26E-05	0.03701
248	0.37626	784.27	595.35	785.21	593.97	250.57	123.05	1.26E-05	0.03776
249	0.41567	785.28	596.36	786.18	594.94	251.03	124.06	1.27E-05	0.03852
250	0.45885	786.29	597.37	787.15	595.91	251.48	125.07	1.27E-05	0.03929
251	0.50611	787.29	598.37	788.12	596.88	251.93	126.07	1.28E-05	0.04007
252	0.55780	788.29	599.37	789.09	597.85	252.39	127.07	1.28E-05	0.04086
253	0.61430	789.29	600.37	790.06	598.82	252.84	128.07	1.29E-05	0.04166
254	0.67600	790.29	601.37	791.02	599.78	253.29	129.07	1.29E-05	0.04248
255	0.74334	791.28	602.36	791.98	600.74	253.74	130.06	1.30E-05	0.04331
256	0.81678	792.27	603.35	792.93	601.69	254.18	131.05	1.30E-05	0.04415
257	0.89682	793.26	604.34	793.89	602.65	254.63	132.04	1.31E-05	0.04500
258	0.98398	794.24	605.32	794.84	603.60	255.08	133.02	1.31E-05	0.04586
259	1.07884	795.22	606.30	795.79	604.55	255.52	134.00	1.32E-05	0.04673
260	1.18200	796.20	607.28	796.73	605.49	255.97	134.98	1.32E-05	0.04762
261	1.29411	797.18	608.26	797.67	606.43	256.41	135.96	1.33E-05	0.04852
262	1.41587	798.15	609.23	798.61	607.37	256.86	136.93	1.33E-05	0.04943
263	1.54802	799.12	610.20	799.55	608.31	257.30	137.90	1.34E-05	0.05036
264	1.69135	800.08	611.16	800.48	609.24	257.74	138.86	1.34E-05	0.05129
265	1.84671	801.04	612.12	801.41	610.17	258.18	139.82	1.35E-05	0.05224
266	2.01500	802.00	613.08	802.34	611.10	258.62	140.78	1.35E-05	0.05321
267	2.19718	802.96	614.04	803.26	612.02	259.06	141.74	1.36E-05	0.05418
268	2.39427	803.91	614.99	804.18	612.94	259.50	142.69	1.36E-05	0.05517
269	2.60736	804.86	615.94	805.10	613.86	259.93	143.64	1.37E-05	0.05618
270	2.83760	805.81	616.89	806.02	614.78	260.37	144.59	1.37E-05	0.05719
271	3.08623	806.75	617.83	806.93	615.69	260.81	145.53	1.38E-05	0.05822
272	3.35456	807.69	618.77	807.84	616.60	261.24	146.47	1.38E-05	0.05926
273	3.64396	808.63	619.71	808.74	617.50	261.68	147.41	1.38E-05	0.06032
274	3.95592	809.56	620.64	809.64	618.40	262.11	148.34	1.39E-05	0.06139
275	4.29199	810.49	621.57	810.54	619.30	262.54	149.27	1.39E-05	0.06247
276	4.65383	811.42	622.50	811.44	620.20	262.97	150.20	1.40E-05	0.06357
277	5.04319	812.34	623.42	812.33	621.09	263.41	151.12	1.40E-05	0.06469
278	5.46193	813.26	624.34	813.22	621.98	263.84	152.04	1.41E-05	0.06581

a. p_r -reference pressure for Mars is 610 Pa.

Select Thermophysical Properties for Mars (continued)

Temp K	p_{sat}/p_r[a] (over ice)	c_p CO_2	c_v CO_2	c_p^0 Mars atm.	c_v^0 Mars atm.	c speed of sound	c_{vib}	**μ** Mars atm.	$P_\infty * \tau_{VT}$
280	6.39553	815.09	626.17	814.99	623.75	264.70	153.87	1.42E-05	0.06811
281	6.91467	816.00	627.08	815.86	624.63	265.12	154.78	1.42E-05	0.06928
282	7.47175	816.91	627.99	816.74	625.50	265.55	155.69	1.43E-05	0.07046
283	8.06924	817.81	628.89	817.61	626.37	265.98	156.59	1.43E-05	0.07166
284	8.70972	818.71	629.79	818.48	627.24	266.41	157.49	1.44E-05	0.07288
285	9.39592	819.61	630.69	819.35	628.11	266.83	158.39	1.44E-05	0.07411
286	10.13073	820.50	631.58	820.21	628.97	267.26	159.28	1.45E-05	0.07535
287	10.91719	821.39	632.47	821.07	629.83	267.68	160.17	1.45E-05	0.07661
288	11.75850	822.27	633.35	821.92	630.68	268.10	161.05	1.46E-05	0.07789
289	12.65803	823.15	634.23	822.78	631.54	268.53	161.93	1.46E-05	0.07918
290	13.61934	824.03	635.11	823.62	632.38	268.95	162.81	1.47E-05	0.08048
291	14.64616	824.91	635.99	824.47	633.23	269.37	163.69	1.47E-05	0.08181
292	15.74242	825.78	636.86	825.31	634.07	269.79	164.56	1.48E-05	0.08315
293	16.91225	826.65	637.73	826.15	634.91	270.21	165.43	1.48E-05	0.08450
294	18.16000	827.51	638.59	826.98	635.74	270.63	166.29	1.49E-05	0.08587
295	19.49021	828.37	639.45	827.82	636.58	271.05	167.15	1.49E-05	0.08726
296	20.90769	829.23	640.31	828.64	637.40	271.47	168.01	1.50E-05	0.08866
297	22.41745	830.08	641.16	829.47	638.23	271.89	168.86	1.50E-05	0.09008
298	24.02476	830.93	642.01	830.29	639.05	272.30	169.71	1.51E-05	0.09151
299	25.73515	831.78	642.86	831.11	639.87	272.72	170.56	1.51E-05	0.09297
300	27.55440	832.62	643.70	831.92	640.68	273.14	171.40	1.52E-05	0.09444

a. p_r -reference pressure for Mars is 610 Pa.

B. MATLAB Script

Mars Thermophysical Properties

Saturated vapor pressures, cp's, cv's, mu's,for a range of T

```
% molar mass
Mco2 = 0.9532*0.04401;
Mn2 = 0.027*0.028013;
Marg = 0.016*0.039948;
Mo2 = 0.0013*0.03199;
Mco = 0.0008*0.02801;
Mh2o = 0.0003*0.01802;      % @ 0.03%
Mh2oa = 0.0008*0.01802;    % @ 0.08%
Mh2ob = 0.0012*0.01802;    % @ 0.12%
Mmair3 = Mco2+Mn2+Marg+Mo2+Mco+Mh2o;
Mmair8 = Mco2+Mn2+Marg+Mo2+Mco+Mh2oa;
Mmair12 = Mco2+Mn2+Marg+Mo2+Mco+Mh2ob;

% spec gas constants
Ru = 8.3145;
Rmair = Ru/Mmair3;      % @ 0.03%
Rmair1 = Ru/Mmair8; % @ 0.08%
Rmair2 = Ru/Mmair12; % @ 0.12%
Rdair = Ru/(Mco2+Mn2+Marg+Mo2+Mco);
Rco2 = 188.92;
Rn2 = 296.8;
Rarg = 208.13;
Ro2 = 259.84;
Rco = 296.84;
Rh2o = 461.52;

% mass fractions
wco2 = Mco2/Mmair3;
wn2 = Mn2/Mmair3;
warg = Marg/Mmair3;
wo2 = Mo2/Mmair3;
wco = Mco/Mmair3;
wh2o3 = Mh2o/Mmair3;         % 0.03%
wh2o8 = Mh2oa/Mmair8;     % 0.08%
wh2o12 = Mh2ob/Mmair12;  % 0.12%

% Cp and Cv non-temp dependent components
Cp_n2 = (7/2)*Rn2;
Cv_n2 = (5/2)*Rn2;
Cp_o2 = (7/2)*Ro2;
Cv_o2 = (5/2)*Ro2;
Cp_co = (7/2)*Rco;
Cv_co = (5/2)*Rco;
Cp_ar = (5/2)*Rarg;
Cv_ar = (3/2)*Rarg;
Cp_h2o = 1853; % J/kg*K
```

```
Cv_h2o = Cp_h2o-Rh2o;
% Sum Cp's and Cv's
SumCp3 = ((Cp_n2*wn2)+(Cp_o2*wo2)+(Cp_co*wco)+(Cp_ar*warg)+(Cp_h2o*wh2o3));
SumCv3 = ((Cv_n2*wn2)+(Cv_o2*wo2)+(Cv_co*wco)+(Cv_ar*warg)+(Cv_h2o*wh2o3));

SumCp8 = ((Cp_n2*wn2)+(Cp_o2*wo2)+(Cp_co*wco)+(Cp_ar*warg)+(Cp_h2o*wh2o8));
SumCv8 = ((Cv_n2*wn2)+(Cv_o2*wo2)+(Cv_co*wco)+(Cv_ar*warg)+(Cv_h2o*wh2o8));

SumCp12 = ((Cp_n2*wn2)+(Cp_o2*wo2)+(Cp_co*wco)+(Cp_ar*warg)+(Cp_h2o*wh2o12));
SumCv12 = ((Cv_n2*wn2)+(Cv_o2*wo2)+(Cv_co*wco)+(Cv_ar*warg)+(Cv_h2o*wh2o12));
```

T Dependent Calculations

```
for k=1:numel(T)
    % Psats And T
    [liq,ice]=goffgratch65(T(k));

        vp_liq(k) = liq;

        vp_ice(k) = ice;

        Temp(k) = T(k);

    % Specific Heat of CO2 and Mars in J/kg-K
    Cpc2(k) = Rco2*(5/2+1+2*((960/T(k))^2)*((exp(960/T(k)))/((exp(960/T(k))-1))^2));
    Cvc2(k) = Cpc2(k)-Rco2;
    Cvib(k) = Rco2*2*((960/T(k))^2)*((exp(960/T(k)))/((exp(960/T(k))-1))^2);

    % globally averaged H2O - 0.03%
    Cpmars3(k) = ((Cpc2(k)*wco2)+SumCp3);
    Cvmars3(k) = ((Cvc2(k)*wco2)+SumCv3);
    Cpinf3(k) = (Rco2*7/2*wco2)+SumCp3;
    Cvinf3(k) = ((Rco2*7/2-Rco2)*wco2)+SumCv3;
    gamma3(k) = Cpmars3(k)/Cvmars3(k);

    % seasonal average H2O @ 68 deg N Lat - 0.08%
    Cpmars8(k) = ((Cpc2(k)*wco2)+SumCp8);
    Cvmars8(k) = ((Cvc2(k)*wco2)+SumCv8);
    Cpinf8(k) = (Rco2*7/2*wco2)+SumCp8;
    Cvinf8(k) = ((Rco2*7/2-Rco2)*wco2)+SumCv8;
    gamma8(k) = Cpmars8(k)/Cvmars8(k);

    % seasonal average H2O @ 68 deg N Lat - 0.12%
    Cpmars12(k) = ((Cpc2(k)*wco2)+SumCp12);
    Cvmars12(k) = ((Cvc2(k)*wco2)+SumCv12);
    Cpinf12(k) = (Rco2*7/2*wco2)+SumCp12;
    Cvinf12(k) = ((Rco2*7/2-Rco2)*wco2)+SumCv12;
    gamma12(k) = Cpmars12(k)/Cvmars12(k);

   % Relaxation Strength
   % multiply by (1-xh) for RH normalized
    relax3(k) = Rmair*Cvib(k)/(Cpinf3(k)*Cvmars3(k));          % @ 0.03%
    relax8(k) = Rmair1*Cvib(k)/(Cpinf8(k)*Cvmars8(k));        % @ 0.08%
    relax12(k) = Rmair2*Cvib(k)/(Cpinf12(k)*Cvmars12(k));  % @ 0.12%
```

```
   % Dynamic viscosity of Mars
   %    using Sutherland's Formula;   mu=mu0*((To+C)/(T+C))*(T/To)^(3/2)
   %    with gas specific Sutherland's constants(C) and ref T and mu's
   %    in kg/m-s
    mu_co2(k) = 1.48e-5*((293.15+240)/...
        (T(k)+240))*((T(k)/293.15)^1.5);
    mu_n2(k) = 1.781e-5*((300.55+111)/...
        (T(k)+111))*((T(k)/300.55)^1.5);
    mu_ar(k) = 2.125e-5*((273.16+144.4)/...
        (T(k)+144.4))*((T(k)/273.16)^1.5);
    mu_o2(k) = 2.018e-5*((292.25+127)/...
        (T(k)+127))*((T(k)/292.25)^1.5);
    mu_co(k) = 1.72e-5*((288.15+118)/...
        (T(k)+118))*((T(k)/288.15)^1.5);
    mu_h2o(k) = (9.25e-5*((T(k)/300)^1.1))/10;

   % globally averaged H2O - 0.03%
    mu_mars3(k) =
((mu_co2(k)*.9532*((Mco2)^.5))+(mu_n2(k)*.027*((Mn2)^.5))+(mu_ar(k)*.016*((Marg)^.5))+...

(mu_o2(k)*.0013*((Mo2)^.5))+(mu_co(k)*.0008*((Mco)^.5))+(mu_h2o(k)*.0003*((Mh2o)^.5)))/...
        ((.9532*((Mco2)^.5))+(.027*((Mn2)^.5))+(.016*((Marg)^.5))+(.0013*((Mo2)^.5))+...
        (.0008*((Mco)^.5))+(.0003*((Mh2o)^.5)));

   % seasonal average H2O @ 68 deg N Lat - 0.08%
    mu_mars8(k) =
((mu_co2(k)*.9532*((Mco2)^.5))+(mu_n2(k)*.027*((Mn2)^.5))+(mu_ar(k)*.016*((Marg)^.5))+...

(mu_o2(k)*.0013*((Mo2)^.5))+(mu_co(k)*.0008*((Mco)^.5))+(mu_h2o(k)*.0008*((Mh2oa)^.5)))/...
        ((.9532*((Mco2)^.5))+(.027*((Mn2)^.5))+(.016*((Marg)^.5))+(.0013*((Mo2)^.5))+...
        (.0008*((Mco)^.5))+(.0008*((Mh2oa)^.5)));
           % seasonal average H2O @ 68 deg N Lat - 0.12%
    mu_mars12(k) =
((mu_co2(k)*.9532*((Mco2)^.5))+(mu_n2(k)*.027*((Mn2)^.5))+(mu_ar(k)*.016*((Marg)^.5))+...

(mu_o2(k)*.0013*((Mo2)^.5))+(mu_co(k)*.0008*((Mco)^.5))+(mu_h2o(k)*.0012*((Mh2ob)^.5)))/...
        ((.9532*((Mco2)^.5))+(.027*((Mn2)^.5))+(.016*((Marg)^.5))+(.0013*((Mo2)^.5))+...
        (.0008*((Mco)^.5))+(.0012*((Mh2ob)^.5)));

    % Rate Constant k & kb for relaxation times
    A = exp(-60.75/((T(k))^(1/3)));
    B = exp(-78.29/((T(k))^(1/3)));
    C = (.06/(mu_h2o(k)));
    D = 1/101325;      % to convert atm to Pa

    %  Forward and Reverse Rate Constants *mole fraction of each comp.
          % globally averaged H2O - 0.03%
    krate3(k) = ((.937*(.219/((mu_co2(k))*A)))+(.0418*(1.44/((mu_n2(k))*B)))+...
        (.01738*(1.44/((mu_ar(k))*B)))+(.00178*(1.44/((mu_o2(k))*B)))+...
        (.00126*(1.44/((mu_co(k))*B)))+(.00072*C))*D;
    kbrate3(k) = (krate3(k)*exp(-960/T(k)));
          % seasonal average H2O @ 68 deg N Lat - 0.08%
    krate8(k) = ((.936*(.219/((mu_co2(k))*A)))+(.042*(1.44/((mu_n2(k))*B)))+...
```

```
        (.0174*(1.44/((mu_ar(k))*B)))+(.00178*(1.44/((mu_o2(k))*B)))+...
        (.00126*(1.44/((mu_co(k))*B)))+(.001923*C))*D;
    kbrate8(k) = (krate8(k)*exp(-960/T(k)));
           % seasonal average H2O @ 68 deg N Lat - 0.12%
    krate12(k) = ((.935*(.219/((mu_co2(k))*A)))+(.0417*(1.44/((mu_n2(k))*B)))+...
        (.0174*(1.44/((mu_ar(k))*B)))+(.00177*(1.44/((mu_o2(k))*B)))+...
        (.00125*(1.44/((mu_co(k))*B)))+(.0029*C))*D;
    kbrate12(k) = (krate12(k)*exp(-960/T(k)));

    % Relaxation Time Tvt - will need to divide by P
    tvt3(k) = (610/(krate3(k)-kbrate3(k)));      % * by Pr = 610
    tvt8(k) = (610/(krate8(k)-kbrate8(k)));      % * by Pr = 610
    tvt12(k) =(610/(krate12(k)-kbrate12(k))); % * by Pr = 610

   % P*mole fraction of water vapor for humidity 1-10%
    if T(k) >= 283
        psat=vp_liq(k);  % *Pr of 610Pa
    else
        psat=vp_ice(k); % *Pr of 610Pa
    end
    PXh_1(k) = .01*psat;
    PXh_2(k) = .02*psat;
    PXh_3(k) = .03*psat;
    PXh_4(k) = .04*psat;
    PXh_5(k) = .05*psat;
    PXh_6(k) = .06*psat;
    PXh_7(k) = .07*psat;
    PXh_8(k) = .08*psat;
    PXh_9(k) = .09*psat;
    PXh_10(k) = .10*psat;
    PXh_20(k) = .20*psat;
    PXh_30(k) = .30*psat;
    PXh_40(k) = .40*psat;
    PXh_50(k) = .50*psat;
    PXh_60(k) = .60*psat;
    PXh_70(k) = .70*psat;
    PXh_80(k) = .80*psat;
    PXh_90(k) = .90*psat;
    PXh_100(k) = psat;


% Speed of sound
c3(k) = (gamma3(k)*Rmair*T(k))^0.5;
c8(k) = (gamma8(k)*Rmair1*T(k))^0.5;
c12(k) = (gamma12(k)*Rmair2*T(k))^0.5;
end
```

Script for Relative Humidity Calculations

RH for 4 Phoenix Dust Devils

```
RH_liq = zeros(1,4);
RH_ice = zeros(1,4);
delP = [2.58 3.56 2.37 2.51];
Tinf = [240 240 228 227];
Pinf = [765.4 752.5 739.5 727];
rho = zeros(1,4);
Sol = [90 95 118 136];
mw = 43.44;
Rmair1 = 191.4713; % @ 0.08%
Rmair2 = 191.4395; % @ 0.12%
Rdair = 191.5349;
Rvap = 461.52;
```

Calculation loop for 4 DD cases

```
for k=1:4
    if k==1
      T=240; P=765.4;
      TES = 65; % H2O column in precipitable microns
      Rmair = Rmair2;    % @ 0.12% H2O
      ztop = 13; % condensation height
      cp=778.02;
    elseif k==2
        T=240; P=752.5;
        TES = 60; % H2O column in precipitable microns
        Rmair = Rmair2;  % @ 0.12% H2O
        ztop = 13; % condensation height
        cp=778.02;
    elseif k==3
        T=228; P=739.5;
        TES = 50; % H2O column in precipitable microns
        Rmair = Rmair1;  % @ 0.08% H2O
        ztop = 11; % condensation height
        cp=765.95;
    elseif k==4
        T=227; P=727;
        TES = 45; % H2O column in precipitable microns
        Rmair = Rmair1;   % @ 0.08% H2O
        ztop = 10; % condensation height
        cp=764.94;
    end
[liq,ice]=goffgratch65(T);

psat_l = liq*610;  % * by Pr of 610Pa
psat_i = ice*610; % * by Pr of 610Pa
```

```
% VMR based RH Calc
nh2o = (.001*TES)/(0.01802*(1.661e-24));  % # of H2O molecules/m^2
epsilon = (Rdair/Rvap);

L=-3.74/cp;
Qo=nh2o/((P)*(1-(1+(L/T)*(ztop*1000))^(-3.74/(L*Rmair)))*(3.7114e24)); % adiabatic barometric
formula
Qsat_l = (epsilon*psat_l)/((P-psat_l+epsilon*psat_l));  % over liq
Qsat_i = (epsilon*psat_i)/((P-psat_i+epsilon*psat_i));  % over ice

RH_liq(k) = 100*(Qo/Qsat_l);
RH_ice(k) = 100*(Qo/Qsat_i);

% Density Calc
rho(k) = P/(T*Rmair);
end
```

Script for Saturation Vapor Pressures

```
% the purpose of this function is to calculate the saturation vapor pressure over
%ice and liquid water from the goff-gratch formulation in Pa For Mars-
%Boiling point 283.16

function [e_l,e_i]=goffgratch65(T)

a1=10.79586;
a2=(1-(273.16/T));
a3=-5.02808;
a4=log10(T/273.16);
a5=1.50474e-4;
a6=(1-(10.^(-8.29692*((T/273.16)-1))));
a7=0.42873e-3;
a8=(1-10.^(-4.76955*((273.16/T)-1)));
a9=log10(611.657);


e_l = (10.^((a1*a2)+(a3*a4)+(a5*a6)+(a7*a8)+a9))*(610/101325);


b1=-9.096936;
b2=((273.16./T)-1);
b3=-3.56654;
b4=log10(273.16./T);
b5=0.876817;
b6=(1-(T./273.16));
b7=log10(611.657);

e_i = (10.^((b1*b2)+(b3*b4)+(b5*b6)+b7))*(610/101325);

end
```

Published with MATLAB® R2019a

VITA

Shelly Cahoon Mann

Old Dominion University
Department of Mechanical and Aerospace Engineering
238 Kaufman Hall
Norfolk, VA 23529

EDUCATIONAL BACKGROUND

M.S. in Aerospace Engineering — May 2021
Old Dominion University, Norfolk, VA

B.S. in Mechanical Engineering — May 1995
Emphasis: Power Systems and Energy Conversion
Old Dominion University, Norfolk, VA

PUBLICATIONS

Mann, S., Weinmann, M., Effort, E. 2019. *A Multi-University Small Satellite Design Course: Systems Engineering Approach.* AIAA 2019-3466.